



## OPEN ACCESS

## EDITED BY

Fei Xue,  
Hohai University, China

## REVIEWED BY

Leilei Dong,  
University of Science and Technology  
Beijing, China  
Qihai Shu,  
China University of Geosciences, China  
Xiangguo Guo,  
Inner Mongolia University of  
Technology, China

## \*CORRESPONDENCE

Zhao-Lu Zhang,  
✉ zhzh@sdut.edu.cn

## SPECIALTY SECTION

This article was submitted to Economic  
Geology,  
a section of the journal  
Frontiers in Earth Science

RECEIVED 30 October 2022

ACCEPTED 06 December 2022

PUBLISHED 10 January 2023

## CITATION

Cai W-Y, Zhang Z-L, Liu X, Gao J-L,  
Ma M, Li Y, Song Y-X and Li Z-S (2023),  
Metallogeny of the Yi'nan Tongjing  
Au–Cu skarn deposit, Luxi district, North  
China Craton: Perspective from in-suit  
trace elements, sulfur and lead isotopes  
of sulfides.  
*Front. Earth Sci.* 10:1084212.  
doi: 10.3389/feart.2022.1084212

## COPYRIGHT

© 2023 Cai, Zhang, Liu, Gao, Ma, Li,  
Song and Li. This is an open-access  
article distributed under the terms of the  
[Creative Commons Attribution License  
\(CC BY\)](https://creativecommons.org/licenses/by/4.0/). The use, distribution or  
reproduction in other forums is  
permitted, provided the original  
author(s) and the copyright owner(s) are  
credited and that the original  
publication in this journal is cited, in  
accordance with accepted academic  
practice. No use, distribution or  
reproduction is permitted which does  
not comply with these terms.

# Metallogeny of the Yi'nan Tongjing Au–Cu skarn deposit, Luxi district, North China Craton: Perspective from in-suit trace elements, sulfur and lead isotopes of sulfides

Wen-Yan Cai<sup>1,2</sup>, Zhao-Lu Zhang<sup>1\*</sup>, Xiao Liu<sup>1</sup>, Ji-Lei Gao<sup>3</sup>,  
Ming Ma<sup>3</sup>, Yadong Li<sup>3</sup>, Ying-Xin Song<sup>4</sup> and Zeng-Sheng Li<sup>4</sup>

<sup>1</sup>School of Resources and Environmental Engineering, Shandong University of Technology, Zibo, China, <sup>2</sup>MNR Key Laboratory for Exploration Theory and Technology of Critical Mineral Resources, China University of Geosciences, Beijing, China, <sup>3</sup>Shandong Provincial No. 1 Exploration Institute of Geology and Mineral Resources, Ji'nan, China, <sup>4</sup>Key Laboratory of Gold Mineralization Processes and Resource Utilization MNR, Ji'nan, China

Gold–Cu skarn deposits are characterized by a diverse mineral assemblage, whose *in-situ* major/trace elements and isotope compositions can provide key constraints to the migration and enrichment of Au during hydrothermal processes. The Yi'nan Tongjing Au–Cu deposit is located in the central part of the Luxi district, and both skarn and Au–Cu ore bodies occur at the contact between the Early Cretaceous diorite porphyry and the Neoproterozoic to Cambrian carbonate rocks. Five stages of mineralization were identified: 1) early skarn (garnet–diopside–wollastonite); 2) late skarn (magnetite–epidote–actinolite±tremolite); 3) oxide (specularite–hematite); 4) sulfide (pyrite–chalcopyrite–sphalerite–quartz–chlorite); and 5) late quartz–calcite. The mineralization process in the Tongjing Au–Cu deposit was revealed by detailed scanning electron microscope-backscattered electron imaging, electron probe microanalysis, *in-situ* trace element, sulfur and lead isotope analysis. Magnetite is enriched in chalcophile elements (Cu, Zn, Pb), Co and Ni, probably due to hydrothermal overprint. The substitution of As and other elements in the formation of pyrite is conducive to the entry of Au into pyrite. The increase of Se and As contents in pyrite from stage IVa to IVb indicates that the temperature, salinity and oxygen fugacity of the ore-forming fluid decrease while the pH rises, resulting in the unloading of Au. The temperature of Au mineralization based on the Se content in pyrite does not exceed 300°C. Furthermore, V positively correlated with Ti and Ni/Cr ratios  $\geq 1$  in magnetite and most Co/Ni ratios in pyrite  $>10$  all confirm their hydrothermal origins. The restricted sulfur ( $\delta^{34}\text{S}_{\text{V-CDT}} = -0.5\text{--}1.2\text{‰}$ ; mean = 0.4‰) and lead ( $^{206}\text{Pb}/^{204}\text{Pb} = 17.323\text{--}17.383$ ;  $^{207}\text{Pb}/^{204}\text{Pb} = 15.424\text{--}15.452$ ;  $^{208}\text{Pb}/^{204}\text{Pb} = 37.367\text{--}37.454$ ) isotopic compositions suggest that the deep magma provided the primary mineralized material, accompanied by a relatively small amount of shallow crustal material. The Yi'nan Tongjing Au–Cu skarn deposit was formed in the Early Cretaceous, which is an important metallogenic response to the strong decratonization of the North China Craton induced by the paleo-Pacific Plate

roll-back. This study shows that there is a large potential of Early Cretaceous skarn mineralization in the Luxi district.

#### KEYWORDS

*in-situ* trace elements analyses, *in-situ* sulfur and lead isotopes, Au precipitation mechanism, Yi'nan Tongjing, skarn deposit, Luxi district

## 1 Introduction

Skarn deposits are an important resource of Au, Ag, Pb, Zn, W, Sn, Fe, and Cu and other metals on a global scale (Einaudi et al., 1981; Hedenquist and Lowenstern, 1994; Meinert et al., 2005; Chen et al., 2007; Chang et al., 2019; Shu et al., 2021; Niu et al., 2022). Skarn deposits, also known as contact metasomatic deposits, form at the contact between intermediate-acid intrusions and carbonate strata (Meinert et al., 2005; Shu et al., 2017; Chang et al., 2019). It has experienced a complex mineralization process (magma/fluid-rock interaction), resulting in a diverse mineral assemblage (Meinert, 1992; Meinert et al., 2005). Minerals, especially mineralization-related (e.g., pyrite, chalcopyrite and magnetite; Cook et al., 2009; Deditius et al., 2014; Nadoll et al., 2014; George et al., 2018a), can be used to reveal the key mineralization information such as ore-forming temperature, elemental substitution and physicochemical conditions as they often are treated as a recorder of mineralization processes. Most types of Au deposits (e.g., orogenic-, epithermal-, intrusion-related, and carlin-type; Groves et al., 1998; Thompson et al., 1999; Hedenquist et al., 2005; Baker et al., 2006; Goldfarb and Groves, 2015) are relatively simple in mineral assemblages, mainly pyrite and chalcopyrite, where only gold-bearing pyrite can constrain the detailed mineralization process (Sung et al., 2009; Fougereuse et al., 2017; Hastie et al., 2020; Chinnasamy et al., 2021). On the other hand, skarn Au deposits have a wide range of mineral assemblages and the major and trace elements of these minerals record a wealth of mineralization information, which helps us to better understand the ore-forming mechanism.

The Luxi district is located in the eastern part of North China Craton (NCC) (Figure 1), and hosts a range of Fe and Au–Cu skarn deposits (Figure 2). These deposits are closely associated with Early Cretaceous intermediate magmatic rocks (diorite and/or diorite porphyry; Xu et al., 2007; Wang et al., 2011; Duan et al., 2020). The Yi'nan Tongjing is a representative Au–Cu deposit in the district. Previous studies mainly focused on fluid inclusions, bulk-ore C–H–O–S–Pb–He–Ar isotopes, zircon U–Pb and whole-rock geochemistry (Qiu et al., 1996; Dong, 2008; Gu et al., 2008; Li et al., 2009; Wang, 2010; Li et al., 2011; Tian et al., 2015; Zhu et al., 2018), revealing that fluid immiscibility led to the precipitation of mineralized material, but the physicochemical conditions for occurrence, migration and

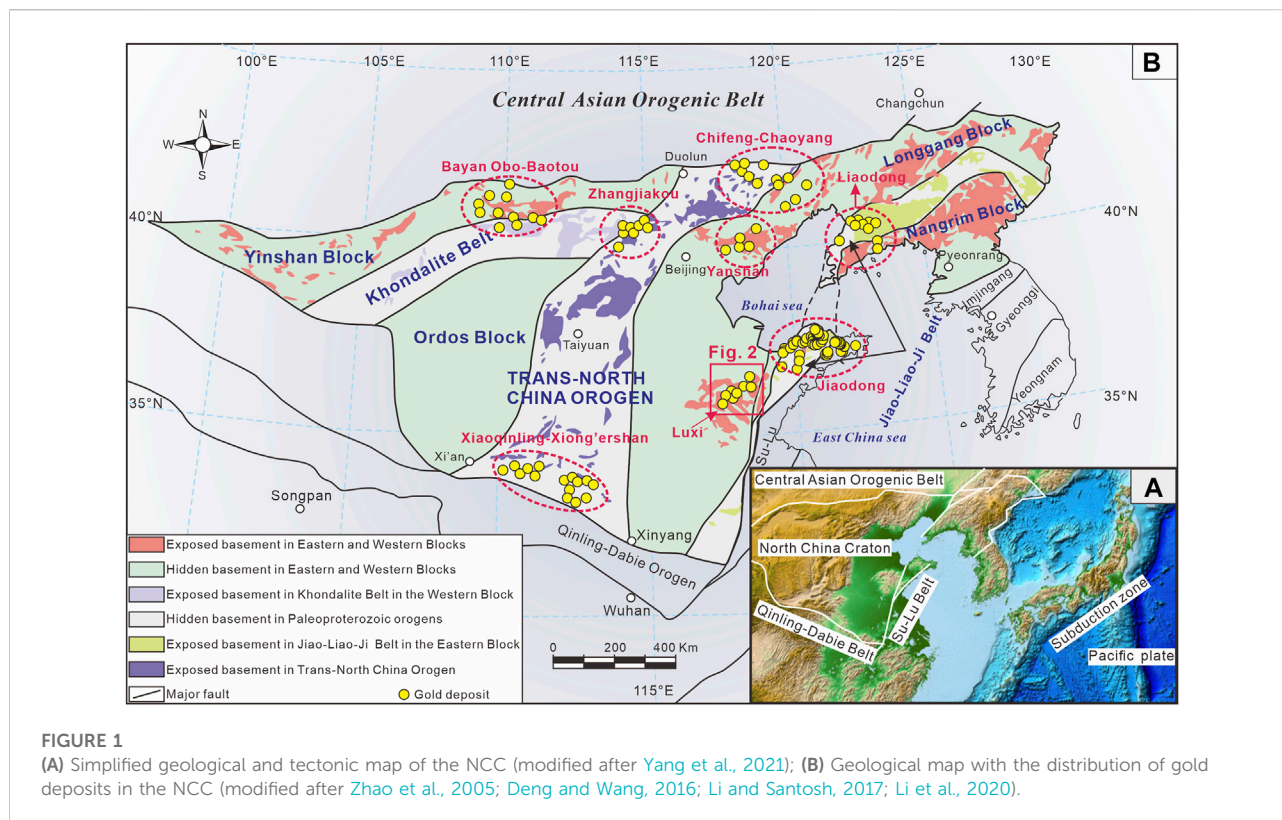
unloading of ore-forming elements are still unclear. The wide range of sulfur and lead isotopic compositions of metal minerals makes it difficult to determine the source of the ore-forming material, and lacks sufficient spatial resolution to reveal the possible multi-stage mineralization processes.

In this study, the possible substitution mechanism between elements, elemental behavior during mineralization and key controlling factors were investigated, and the source of ore-forming material was also constrained. Based on detailed field geological investigations and ore texture, electron probe microanalysis and *in-situ* laser ablation-inductively coupled plasma-mass spectrometry (LA-ICP-MS) trace element composition analyses were performed on metal minerals (magnetite, pyrite, sphalerite and chalcopyrite), and *in-situ* LA-ICP-MS sulfur and lead isotope analyses were conducted on pyrite and chalcopyrite.

## 2 Geological setting

The NCC is adjacent to the Central Asian Orogenic Belt in the north, and the Qinling–Dabie Su–Lu Orogenic Belt in the south (Figure 1). The NCC is the oldest and largest craton in China (Zhai and Santosh, 2011; Zhao and Cawood, 2012) and eventually cratonized and stabilized at approximately 1.85 Ga (Zhao et al., 2001; Santosh, 2010; Zhai, 2011). During the Mesozoic, the nature and thickness of the subcontinental lithospheric mantle beneath the eastern NCC were changed (Menzies et al., 1993; Xu, 2001; Zhu et al., 2011; Yang et al., 2012), which triggered extensive tectonism, magmatism, and large-scale metal mineralization (e.g., Au, Fe and Cu) (Mao et al., 2003; Wu et al., 2005a; 2005b; Zhu et al., 2012; Zeng et al., 2013, 2020). The NCC holds approximately 50% Au production and proven reserves of China (Deng and Wang, 2016; Yang et al., 2021). These Au deposits are mainly distributed in the Xiaoqinling–Xiong'ershan, Liaodong, Chifeng–Chaoyang, Yanshan, Zhangjiakou, Bayan Obo–Baotou, Jiaodong and Luxi districts (Figure 1B).

The Luxi terrane is dominantly composed of Neoproterozoic gneisses, amphibolites and TTGs and Paleoproterozoic granitoids (Song et al., 2001; Wan et al., 2011; Wu et al., 2013), which are overlain by Neoproterozoic Tumen Group (littoral clastic and carbonate rocks) and Paleozoic to Cenozoic sequences (Guo et al., 2014; Deng et al., 2018). The Paleozoic strata are widely exposed in Luxi, including carbonate,



shale and clastic rocks (Dong, 2008), whilst the Mesozoic to Cenozoic strata mainly consist of terrestrial clastic and volcanic-sedimentary rocks (Niu et al., 2004; Hu et al., 2006).

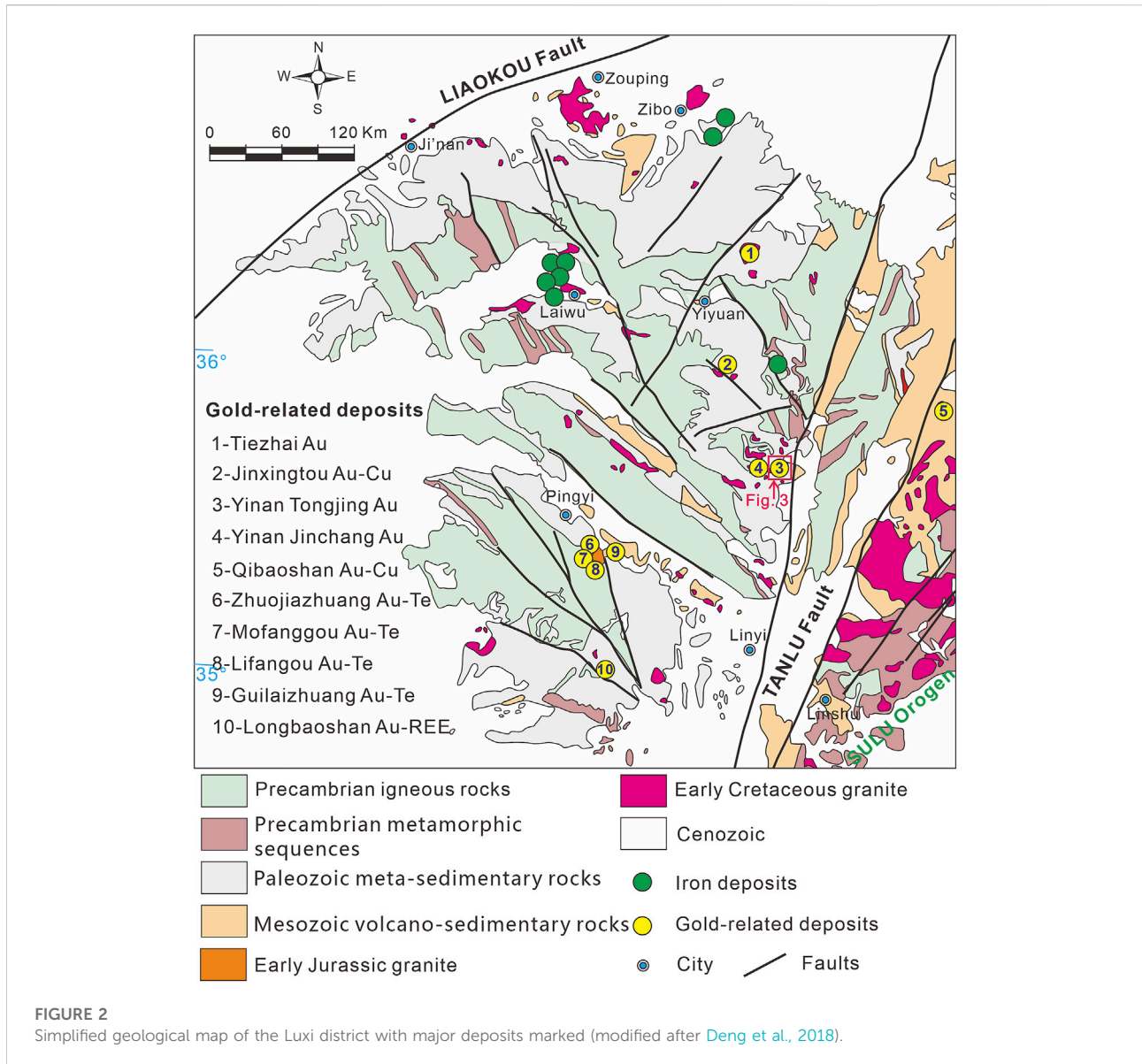
Ninety-five percent of the exposed igneous rocks in Luxi are Precambrian units, and the rest are small-scale Mesozoic intrusive rocks, mainly formed in the Early Jurassic (ca. 185–180 Ma; Lan et al., 2012) and Early Cretaceous (ca. 135–125 Ma; Xu et al., 2004; Yang et al., 2006; 2008; Zhang et al., 2021). The Early Cretaceous magmatism is exemplified by the Laiwu kuangshan and Yi'nan Tongjing intrusive complex (Wang et al., 2011; Duan et al., 2020; Gao et al., 2022). They are mainly composed of diorite and gabbro, with a small amount of granite, which is closely related to the large-scale Fe and Au deposits in the area (Hu et al., 2010; Wang, 2010; Duan and Li, 2017).

### 3 Deposit geology

The Yi'nan Tongjing Au-Cu deposit is located 8 km north of Yi'nan County in western Shandong Province, China, which is mainly composed of six ore segments: Shanzhijian, Gongquan, Jinlong, Gongquandong, Duijinshan and Tonghanzhuang (Figure 3).

Cambrian sequences are widely exposed in the ore district (Figure 3), including Changqing Group

(Zhushadong and Mantou formations) and Jiulong Group (Zhangxia and Gushan formations), which are the main ore-hosting rocks (Figure 4A; Liu et al., 2014). They consist of limestone, dolomite, sandstone and shale (Figure 4A; Dong, 2008), whilst these rocks extend along NW–SE (300°) and incline to the SW at angles of 10–30° (SDGG, 2008). The Archean Taishan Group (metabasic volcanic–sedimentary rocks; Guo et al., 2014) is overlain by the Proterozoic Tumen Group (Tongjiazhuang Formation) in unconformable contact (Figure 4A; Dong, 2008). The Tongjiazhuang Formation includes shale intercalated with thin limestone, in which skarnization occurred (Figure 4A; SDGM, 2015). Faults in Tongjing are affected by the Tan-lu fault, mainly including NNE-, NW-, and SN-trending faults (Figure 3). The NNE- and NW-trending faults are characterized by multi-stage activities, which are filled with mineralized quartz or carbonate veins (SDGG, 2008). Besides, the NNE-trending faults were cut by NW-trending faults. Magmatic intrusion (e.g., Tongjing intrusive complex) often occurred at the intersections of these two sets of faults (Dong, 2008). Tongjing complex comprises pyroxene/quartz diorite in the middle as xenoliths, a small volume of hornblende diorite porphyry in the west and quartz diorite porphyry distributed around them (Figure 3), which were formed in the Early Cretaceous (136–126 Ma; Xu et al., 2007; Wang, 2010; Wang et al.,



2011; Li et al., 2011; Duan et al., 2020). Diorite is intruded by the diorite porphyry or occurs as xenoliths in the latter, indicating its early emplacement (Duan et al., 2020). Skarnization and Au-Cu mineralization mainly occur in the contact zone between the Tongjing complex and Proterozoic to Cambrian carbonate sequences (Figure 4A) and in the structurally weak zone of the strata (Dong, 2008; SDGG, 2008).

More than ten major ore bodies have been identified in Tongjing, and they are mainly hosted in Neoproterozoic to Cambrian strata or the contact between these strata and diorite porphyry (Figure 4A; SDGM, 2015). The ore bodies occur around intrusive rocks in a circular belt (Dong, 2008), so the trends of the ore bodies vary greatly. The ore bodies are

layered and lenticular (Figure 4B), with lengths of 15–240 m, widths of 0.5–25 m and depths of 200 m (SDGG, 2008). However, the scale of a single Au-Cu ore body is generally small (Figure 4B). For example, the No. 1 ore body is hosted in thin sandstone and shale of the Zhushadong Formation and occurs in layers. The ore body has a strike of  $134^{\circ}$  and dips at  $10\text{--}15^{\circ}$  to the SW. It is approximately 160 m long, 0.5–8.95 m thick, and extends to depths of 150 m. The average grades of Au, Cu and Fe in the ore body are 2.89 g/t, 0.19% and 0.63%, respectively (SDGG, 2008).

Based on field and petrographic observations, five paragenetic stages at Tongjing deposit are recognized: 1) early skarn; 2) late skarn; 3) oxide; 4) sulfide; and 5) late quartz-calcite (Figure 5, Figure 6, Figure 7). The mineral assemblage of the early

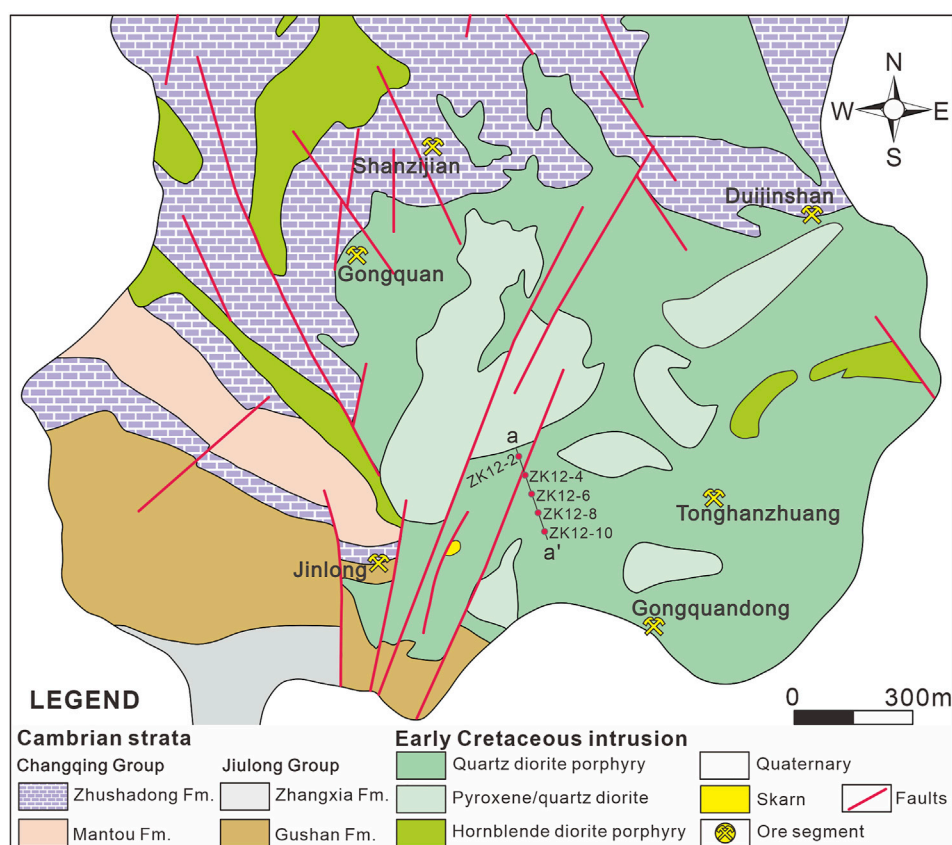


**FIGURE 3**

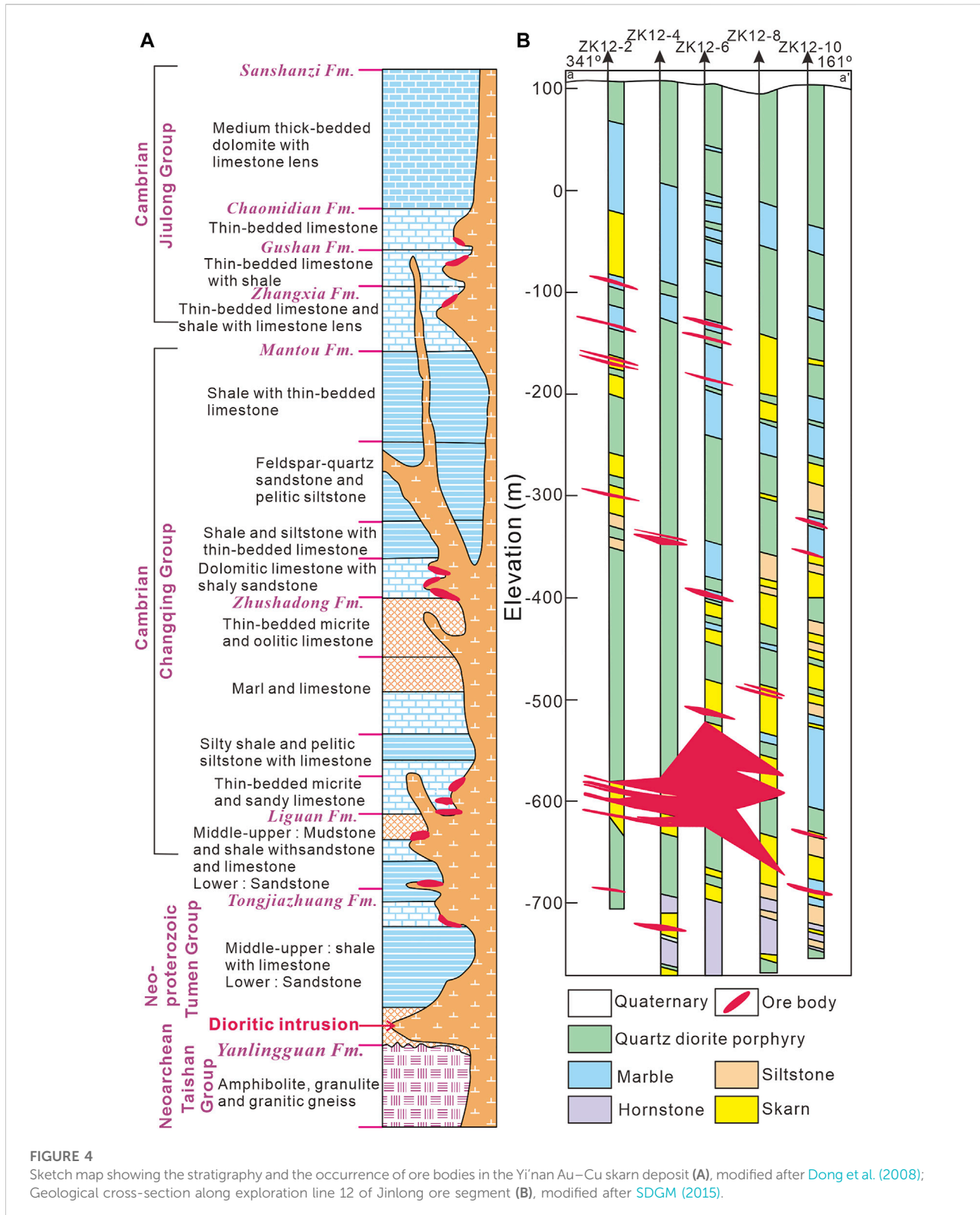
Geological map of the Yinan Tongjing Au–Cu deposit, modified after SDGM (2015) and Duan et al. (2020). The cross section of the exploration line (a–a') is shown in Figure 4B.

skarn stage consists mainly of anhydrous garnet, diopside and wollastonite. They are mainly present in striped, veinlet, and scarce relics in Au–Cu ores (Figures 5F,H). The coarse garnet is replaced by an epidote along the edge (Figure 6K). The wollastonite occurs as long-prismatic and platelike. As the main stage of Fe mineralization, the late skarn is characterized by the occurrence of epidote, tremolite, actinolite and magnetite (Figures 5B,E–G), which are widely developed in strips or blocks. Magnetite and epidote are filled by late pyrite, chalcopyrite and calcite along the gap between particles (Figures 6A,L). The oxide stage is marked by the pervasive occurrence of hematite, specularite and quartz, occurring in veinlets and lumpy, which is superimposed on the early skarn stage. Specularite is mostly acicular and cut by late sulfides or chlorite veins (Figures 5H, 6C), whilst hematite grew along the edge of magnetite. Pyrite and chalcopyrite as well as minor sphalerite and bornite occur in the sulfide stage (Figure 6B). These minerals often replace the skarn minerals (Figures 5B,E), occurring as interstitial fillings or cross-cut veins (Figures 5F,G, 6A). The gangue minerals in this stage include chlorite, quartz, sericite, fluorite and calcite. Chlorite is veined, striped or irregularly shaped and overprinted on the early

reddish brown or dark green hornstone (Figure 5H). This is the main Au–Cu mineralization stage, and the formation of native gold is related to chalcopyrite and pyrite (Figures 6D–G). Gold is wrapped in pyrite and chalcopyrite in granular or irregular shape (Figures 6D,G; Supplementary Figure S1A,B), and occurs along the edge of euhedral pyrite (Figure 6E; Supplementary Figure S1D) or in quartz vein (Figure 6F; Supplementary Figure S1C,E). Stage IV is further divided into two sub-stages: Stage IV-a mainly includes pyrite and minor chalcopyrite, occurring in massive, disseminated or stripped, and quartz is rare in this sub-stage (Figure 5A); Chalcopyrite-pyrite-quartz veins occur in the stage IV-b, and these veins cut through the stage IV-a and earlier stages (Figures 5C,D,F–G). The quartz–calcite veins in stage V are poor in sulfides, and both they and fluorite veins cut early ores (Figure 5I, Figures 6K,L).

## 4 Samples and analytical methods

Twenty-two samples (21YNT01 to 21YNT22) in this investigation were selected from the Jinlong ore segment



526 m level and the Gongquandong ore segment 180 m level. Forty-one polished thin sections with thicknesses of 30 and 50 μm for subsequent mineralogical and geochemical

analyses. Pyrite, chalcopyrite, sphalerite and magnetite from Au-Cu ores were chosen for EPMA, LA-ICP-MS and *in-situ* S and Pb isotope analyses.

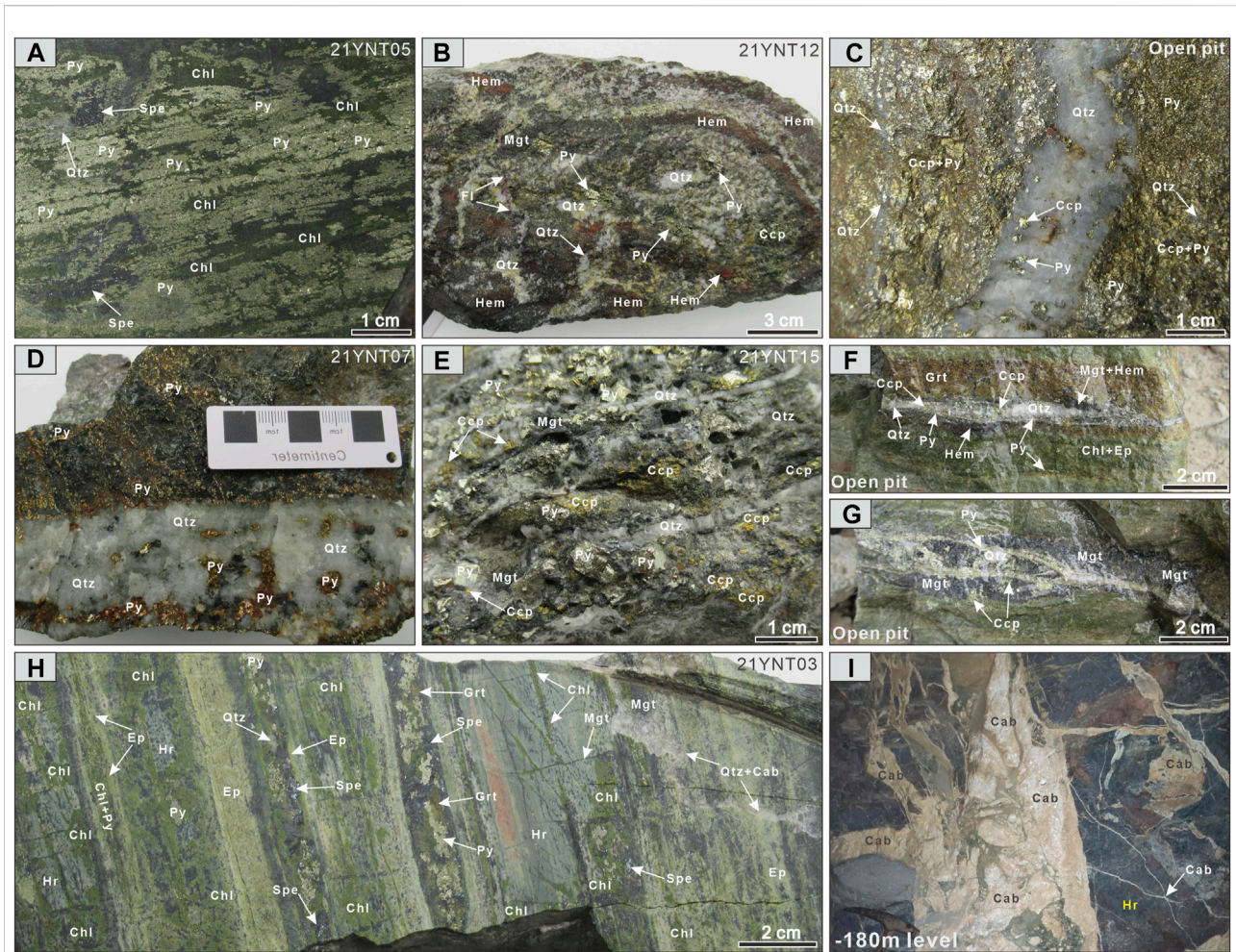


**FIGURE 5**

Photographs of hand specimens from the Tongjiing Au–Cu deposit. **(A)** Striped Au ore with specularite precursor, accompanying chlorite and pyrite; **(B)** Au–Cu ore including chalcopyrite, pyrite and magnetite and hematite relic, cut by later quartz and fluorite veinlets; **(C)** Chalcopyrite–pyrite–quartz vein cutting the massive Au–Cu ore; **(D)** Pyrite–quartz vein cutting the disseminated Au ore; **(E)** Au–Cu ore with magnetite relics, crossed by later quartz veinlets; **(F,G)** Garnet or epidote skarn with magnetite and hematite, cut by chalcopyrite–pyrite–quartz vein; **(H)** Au–Cu ore showing striped sulfides and oxides, reddish and grey hornstone, epidote, chlorite and garnet relic. Most specularite and magnetite are replaced by pyrite *in situ*, the irregular (pyrite–) chlorite veins cutting hornstone or magnetite vein, with late carbonate–quartz vein cutting the ore; **(I)** Multistage carbonate veins cutting early dark grey hornstone. Abbreviations: Cab–carbonate; Ccp–chalcopyrite; Chl–chlorite; Ep–epidote; Fl–fluorite; Grt–garnet; Hem–hematite; Hr–hornstone; Mgt–magnetite; Py–pyrite; Qtz–quartz; Spe–specularite.

#### 4.1 Electron probe microanalysis (EPMA)

Mineral compositions of gold, sulfides and oxides grains were analyzed by a Japan JEOL JXA-8320 electron probe with four wavelength-dispersive spectrometers at Shandong institute of geological sciences, Ji'nan, China. Gold and sulfides analyses were conducted using an accelerating voltage of 20 kV, a beam current of 20 nA and a beam size of 1  $\mu\text{m}$ . Natural pyrite (S, Fe), chalcopyrite (Cu), sphalerite (Zn), galena (Pb), bismuth selenide (Bi, Se), antimony telluride (Te, Sb) and arsenopyrite (As) were used for standardization, while other elements (Co, Ni, Au, Ag) were standardized on metals. The operational voltage was 15 kV, with a beam current of 10 nA, and a diameter of 5  $\mu\text{m}$  for oxides analyses.

The standardized natural minerals and synthetic compounds were followed: magnetite (Fe), almandine (Al), jadeite (Si), diopside (Mg), rutile (Ti), rhodonite (Mn), celestite (Sr), nickel (Ni), vanadium (V), chromium trioxide (Cr), sphalerite (Zn). Raw data ZAF corrections were made with proprietary JEOL software. The minimum detection limit is usually <0.01 wt%.

#### 4.2 LA-ICP-MS *in situ* trace element analysis

Element analysis of mineral in thin sections was conducted by LA-ICP-MS at Nanjing FocuMS Technology Co. Ltd.

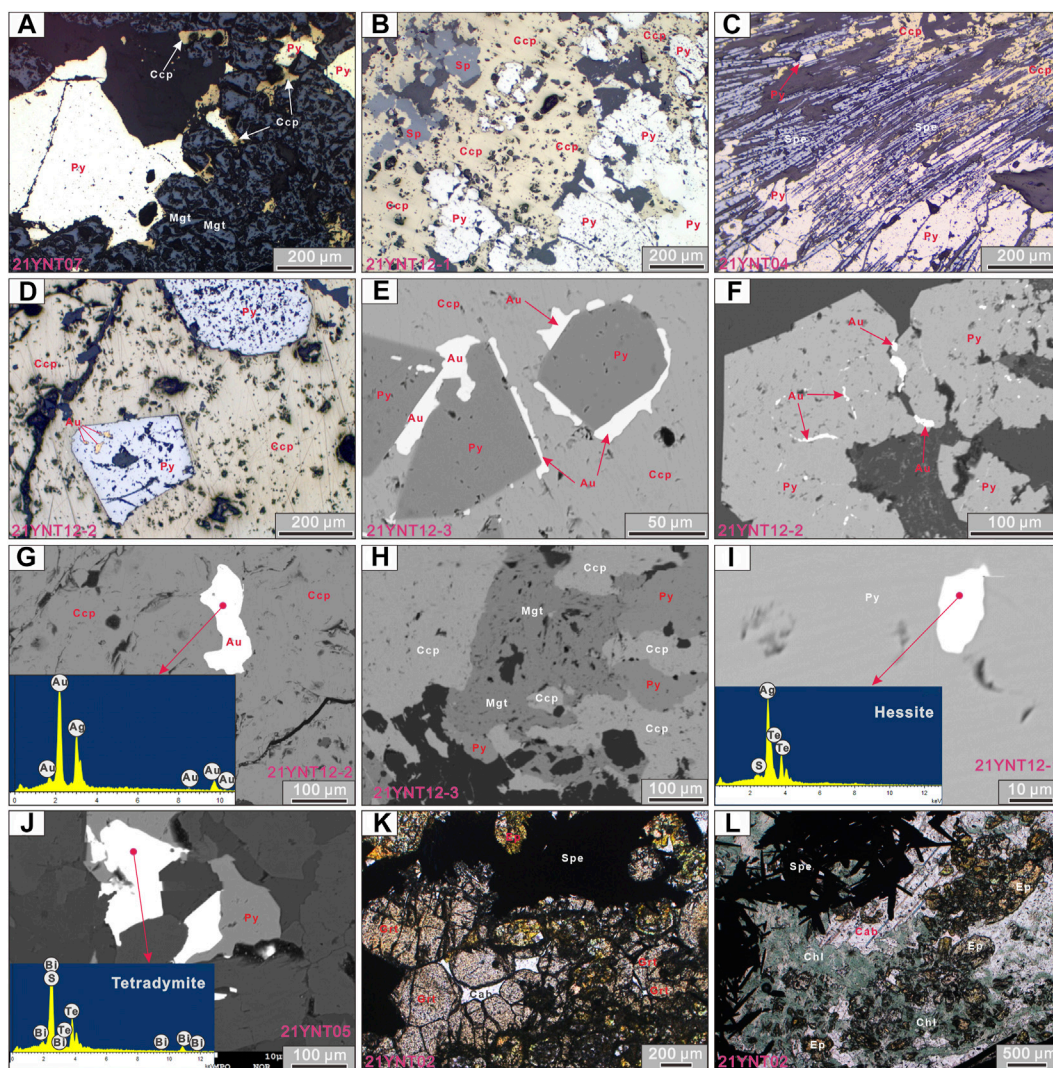


**FIGURE 6**

Photomicrographs of Au–Cu mineralization in Tongjing deposit. (A) Pyrite and chalcopyrite filled along the gap of subhedral magnetite; (B) Pyrite is replaced by chalcopyrite along the edges of pyrite, chalcopyrite overprinted by sphalerite; (C) Acicular specularite filled or replaced by pyrite and chalcopyrite; (D) Natural gold occurring in euhedral pyrite as irregular particles, they wrapped by chalcopyrite; (E) Irregular or granular natural gold grew along the outer edge of euhedral pyrite, they appearing in chalcopyrite in BSE images; (F) Irregular stripped native gold occurring in fissures inside the euhedral pyrite in BSE images; (G) Silver-bearing natural gold wrapped in chalcopyrite in BSE images; (H) Chalcopyrite, pyrite and early residual magnetite occurring in Au–Cu ores; (I) Pyrite containing spindle-shaped hessite; (J) Pyrite and tetradymite growing together; (K) Carbonate veins filled along the gap of euhedral garnet, epidote replacing garnet around the edge of garnet; (L) Epidote, chlorite and carbonate alterations with specularite. Sp–sphalerite; Au–native gold; other abbreviations as for Figure 5.

LA-ICP-MS analyses of metal oxides and sulfides were performed using a Teledyne Cetac Analyte Excite laser-ablation system coupled to an Agilent 7,700× quadrupole ICP-MS. The 193 nm ArF excimer laser was focused on the surface of oxides and sulfides, with a fluence of 6.0 J/cm<sup>2</sup> and 3.0 J/cm<sup>2</sup> respectively. Each acquisition incorporated 20 s background (gas blank), followed by a spot diameter of 40 μm at 6 Hz (oxides) or 5 Hz (sulfides) repetition rate for 40 s. Helium (370 ml/min) was applied as a carrier gas to efficiently transport

aerosol and was mixed with argon (~1.15 L/min) *via* T-connector before entering the ICP torch.

Forty-one isotope signals in sulfide were collected in this experiment, and the values were calculated by using MASS-1 and GSE-1G as an external standard and no internal standard. For oxide, United States Geological Survey basaltic glasses, including BIR-1G, BHVO-2G, BCR-2G and GSE-1G, were used as external calibration standards as these are of the similar matrix as anhydrous silicate. Raw data was performed offline by

Stages Minerals	Early skarn (I)	Late skarn (II)	Oxide (III)	Sulfide (IV)	Quartz–calcite (V)
Garnet	██████████				
Diopside	██████████				
Wollastonite	██████████				
Epidote		██████████	-----		
Tremolite		██████████			
Actinolite		-----			
Magnetite		██████████	██████████		
Muscovite			-----		
Hematite			██████████		
Scheelite			-----		
Chlorite			██████████	██████████	
Chalcopyrite				██████████	
Pyrite				██████████	-----
Native gold				██████████	
Galena				-----	
Bornite				-----	
Sphalerite				██████████	
Quartz			-----	██████████	██████████
Calcite				██████████	██████████
Fluorite					██████████

Main
  Minor
  Locally occurring

**FIGURE 7**  
Mineral paragenesis for the Yi'nan Tongjing Au–Cu deposit.

ICPMSDataCal software (Liu et al., 2008). The precision of each analysis is better than 20% for the most elements.

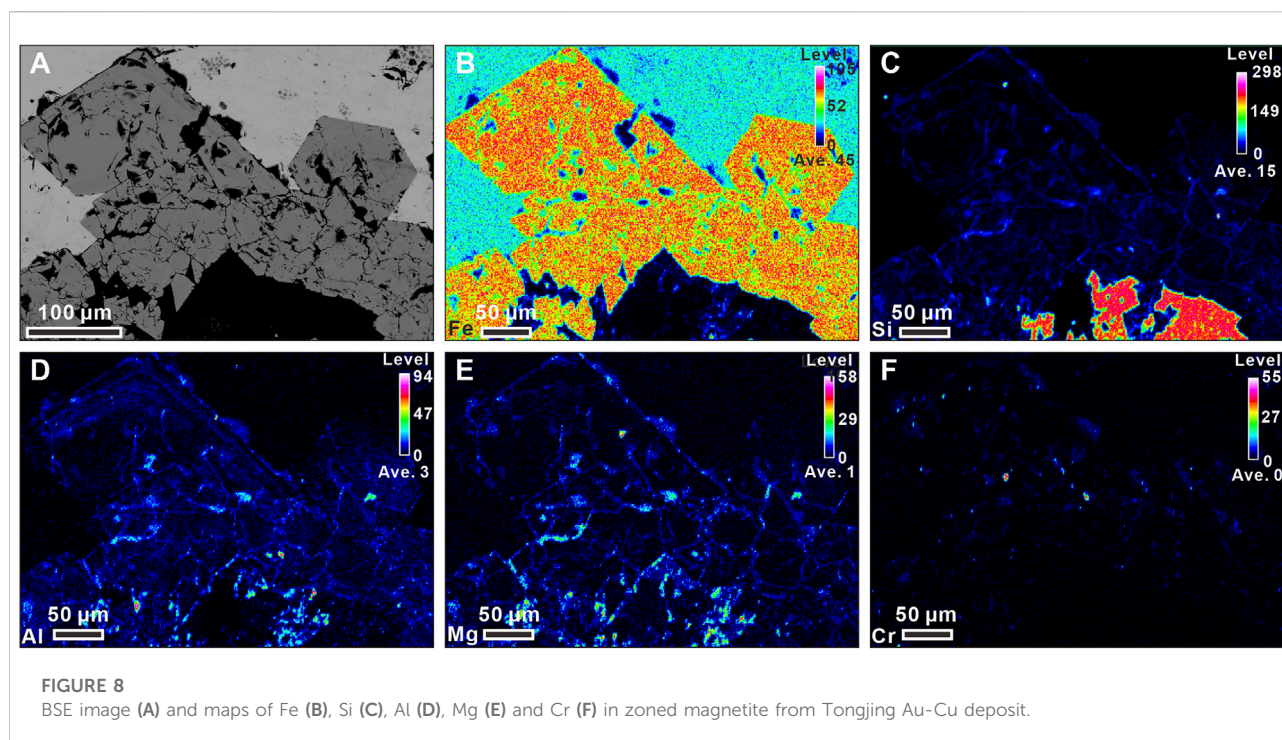
### 4.3 *In-situ* S isotope analysis

*In-situ* sulfur isotope spot analysis of sulfides (pyrite and chalcopyrite) was carried out at Nanjing FocuMS Technology Co. Ltd., utilizing an Analyte Excite laser-ablation system (Bozeman, Montana, United States) and a Nu Plasma II MC–ICP–MS (Wrexham, Wales, United Kingdom). The 193 nm ArF excimer laser was focused on the surface with a spot of 50  $\mu\text{m}$  pit size for chalcopyrite, 33  $\mu\text{m}$  for pyrite and 40  $\mu\text{m}$  for sphalerite, 5 Hz pulse frequency and 2.5 J/cm<sup>2</sup> fluences. The single spot was ablated for 30 s collection of background signal and 35 s data. The integration time of Nu Plasma II was set to 0.3 s (equating to 115 cycles during the 35 s). Natural pyrite Wenshan ( $\delta^{34}\text{S} = +1.1\text{‰}$ ) was used as an external bracketing standard every fourth analysis to ensure precision and account for instrument drift. Pressed powder pellets of pyrite GBW07267 and chalcopyrite GBW07268

( $\delta^{34}\text{S} = +3.6\text{‰}$ ,  $-0.3\text{‰}$  respectively, from the National Research Center for Geoanalysis, China) and fine-grained sphalerite SRM 123 ( $\delta^{34}\text{S} = +17.5\text{‰}$ , from National Institute of Standards and Technology, U.S) were treated as quality control. All measurements are presented relative to CDT, and the long-term reproducibility of  $\delta^{34}\text{S}$  is better than 0.6‰ (1 Standard Deviation).

### 4.4 *In-situ* Pb isotope analysis

The *in-situ* lead isotope analyses of pyrite were performed on a Neptune Plus MC–ICP–MS (Thermo Fisher Scientific, Bremen, Germany) equipped with a Geolas HD excimer ArF laser ablation system (Coherent, Göttingen, Germany) at the Wuhan Sample Solution Analytical Technology Co., Ltd., Hubei, China. The spot diameter ranged from 60 to 90  $\mu\text{m}$  dependent on Pb signal intensity, with 8 Hz pulse frequency and 6.0 J/cm<sup>2</sup> fluence. A new signal-smoothing and mercury-removing device were used downstream from the sample cell to efficiently eliminate the short-term variation of the signal and remove the mercury from



the background and sample aerosol particles (Hu et al., 2015). Sph-HYLM as an external standard was used to monitor the precision and accuracy of the measurements. The obtained accuracy is estimated to be equal to or better than  $\pm 0.2\text{‰}$  for  $^{208}\text{Pb}/^{204}\text{Pb}$ ,  $^{207}\text{Pb}/^{204}\text{Pb}$ , and  $^{206}\text{Pb}/^{204}\text{Pb}$ , with an external precision of  $0.4\text{‰}$  ( $2\sigma$ ). More detail of the *in-situ* Pb isotopic ratios analysis was described. All data reduction for the MC-ICP-MS analysis of Pb isotope ratios was conducted using “Iso-Compass” software (Zhang et al., 2020).

## 5 Results

### 5.1 Major element compositions analyzed by EPMA

A total of 76 EPMA analyses spots were completed on single particles of metal oxides and sulfides, including 45 spots of pyrite, 12 spots of chalcopyrite, 4 spots of sphalerite from the stage IVa and IVb and 15 spots of magnetite as euhedral-subhedral octahedron in stage II or relics in stage IV. The above EPMA results are listed in Supplementary Table S1.

The Fe content of the magnetite ranged from 65.39 to 71.33 wt%, lower than the stoichiometric value of 72.40 wt%. In general, the trace element contents for the magnetite vary from below detection limits to  $\sim 2$  wt% (Supplementary Table S1). Silicon, Mg and Al contents of magnetite are 0.17–1.70 wt% (avg. 1.24 wt%), 0–0.57 wt% (avg. 0.23 wt%) and 0–0.75 wt%

(avg. 0.36 wt%). EPMA elements mappings of magnetite show the oscillatory variation of Si, Al and Mg (Figure 8), indicating a change in the composition of ore-forming fluid.

Iron and S contents of pyrite are 46.11–46.75 wt% (avg. 46.42 wt%) and 53.32–53.62 wt% (avg. 53.49 wt%) in stage IVa, 40.49–46.78 wt% (avg. 45.38 wt%) and 51.72–53.29 wt% (avg. 53.35 wt%) in stage IVb. The contents of Fe, Cu, S and Zn in chalcopyrite from stage IVb are 28.55–30.12 wt% (avg. 29.64 wt%), 33.39–34.83 wt% (avg. 34.26 wt%), 33.52–35.11 wt% (avg. 34.44 wt%) and 0.01–1.51 wt% (avg. 0.21 wt%), respectively. Zinc and S contents of sphalerite are 51.36–59.13 wt% (avg. 55.73 wt%) and 32.38–32.83 wt% (avg. 32.62 wt%) in stage IVb, with a Fe content of 3.74–7.07 wt% (avg. 4.94 wt%) and a Cu content of 3.54–7.84 wt% (avg. 5.25 wt%).

The fineness [ $1,000 \cdot \text{Au}/(\text{Au}+\text{Ag})$ , by weight; Hough et al. (2009)] of Au grains has been calculated based on EPMA results ( $n = 11$ ), with the detailed data in Supplementary Table S1. The two generations of visible gold have distinct characteristics in mineral assemblage and composition (Supplementary Table S1). Au-1 exhibits irregular droplets and is wrapped by chalcopyrite and euhedral pyrite (Figures 6D,G; Supplementary Figure S1A,B), and the Au content of Au-1 (85.94–97.02 wt%, avg. 91.16 wt%) is significantly higher than that of Au-2 (62.03–84.91 wt%, avg. 71.70 wt%). Au-2 mainly occurs at the edge of pyrite or in pyrite–quartz vein (Figures 6E,F; Supplementary Figure S1C,E), and the Au-2 has a higher Ag content (14.65–29.68 wt%, avg. 24.24 wt%) than the Au-1 (1.51–7.51 wt%, avg. 5.88 wt%). The average fineness of Au-1

and Au-2 is 939.17 (919.65–984.69,  $n = 5$ ) and 745.68 (690.28–852.89,  $n = 6$ ), respectively. According to the gold and silver series mineral classification (Zhang and Chen, 1995), the Au fineness indicates that Au-1 and Au-2 belong to the high-medium temperature Au–Ag series in the Yi'nan Tongjing Au–Cu deposit.

## 5.2 Trace element chemistry by LA–ICP–MS

The 98 individual LA–ICP–MS spots were analyzed for the pyrite, chalcopyrite, sphalerite and magnetite relics from Au–Cu ores. The analytical results are presented in Supplementary Table S2 and Figures 9, 11–13 and Supplementary Figure S1, S2. We selected chalcopyrite and pyrite with no inclusions for analysis to obtain precise results.

### 5.2.1 Magnetite

The lithophile elements in magnetite grains include Na (179–380 ppm, avg. 251 ppm), Mg (27.06–186 ppm, avg. 109 ppm), Al (146–4,427 ppm, avg. 2069 ppm), Si (7,316–116616 ppm, avg. 8,965 ppm), K (202–605 ppm, avg. 371 ppm), Ti (15.44–283 ppm, avg. 113 ppm), Sr (8.04–17.30 ppm, avg. 12.14 ppm) and Ba (5.20–20.60 ppm, avg. 10.15 ppm). Magnetite has a high content of chalcophile elements, including Cu (4.74–1,199 ppm, avg. 216 ppm), Zn (19.51–81.83 ppm, avg. 50.74 ppm), Ga (1.83–13.12 ppm, avg. 7.47 ppm), In (0.38–13.71 ppm, avg. 3.72 ppm) and Pb (9.12–66.76 ppm, avg. 27.82 ppm). The contents of As (319–1,456 ppm, avg. 703 ppm), Ni (39.39–369 ppm, avg. 182 ppm), Cr (12.35–1,416 ppm, avg. 236 ppm), W (5.39–176 ppm, avg. 86.34 ppm) and Mo (6.52–65.48 ppm, avg. 34.77 ppm) in magnetite are relatively high, and the Ca content is lower than the detection limit.

### 5.2.2 Pyrite

Pyrite in stage IVa has large compositional variations (Supplementary Table S2, Figure 9). The contents of Co (75.60–285 ppm, avg. 146 ppm), Ni (1.22–6.01 ppm, avg. 2.99 ppm), As (50.10–104 ppm, avg. 84.20 ppm), Se (1.99–3.36 ppm, avg. 2.64 ppm) and Te (7.55–56.53 ppm, avg. 21.01 ppm) are distinctly higher than other trace elements in pyrite, such as Cu (3.60 ppm), Zn (1.13 ppm) and Au (0.02–0.13 ppm, avg. 0.06 ppm). Compared with pyrite in stage IVa, pyrite in stage IVb contains relatively higher trace elements (Co (350–84521 ppm, avg. 39,259 ppm), Ni (25.06–13117 ppm, avg. 2,408 ppm), Cu (0.55–5,227 ppm, avg. 582 ppm), Se (16.49–215 ppm, avg. 43.26 ppm), Ag (0.24–3,921 ppm, avg. 443 ppm), Bi (0.45–3,641 ppm, avg. 201 ppm), Pb (0.06–7,021 ppm, avg. 271 ppm), Te (1.77–3,877 ppm, avg. 257 ppm), As (1.08–4,899 ppm, avg. 842 ppm), Zn (1.02–28.15 ppm, avg. 4.65 ppm; 309–674 ppm,

avg. 455 ppm), Au (0.05–444 ppm, avg. 28.42 ppm), and Sb (0.07–2.01 ppm, avg. 0.48 ppm)).

### 5.2.3 Chalcopyrite

Trace element data of chalcopyrite from stage IVb are shown in Figure 9. The contents of Zn (3.80–2,799 ppm, avg. 979 ppm), Co (0.36–5,839 ppm, avg. 410 ppm), Ni (0.27–2,451 ppm, avg. 177 ppm), Ag (8.80–72.34 ppm, avg. 34.02 ppm), Pb (1.50–42.00 ppm, avg. 20.54 ppm), Bi (2.45–31.07 ppm, avg. 11.42 ppm) and Se (12.23–28.61 ppm, avg. 21.90 ppm) from chalcopyrite are distinctly higher than other trace elements (Figure 9). The contents of Ti, As, Cd, In, Sn, Sb, Te and Au from chalcopyrite are 0.87–2.34 ppm (avg. 1.45 ppm), 1.15–111 ppm (avg. 32.86 ppm), 0.30–12.05 ppm (avg. 4.91 ppm), 2.00–3.74 ppm (avg. 3.11 ppm), 0.71–3.40 ppm (avg. 1.70 ppm), 0.23–1.91 ppm (avg. 0.57 ppm), 1.22–28.62 ppm (avg. 8.26 ppm), and 0.03–1.09 ppm (avg. 0.22 ppm), respectively (Supplementary Table S2, Figure 9).

## 5.3 Sulfur and lead isotope compositions

Sulfur isotope compositions were determined in chalcopyrite and pyrite by LA–MC–ICP–MS, and the results are listed in Supplementary Table S3, Supplementary Figure S2 and plotted in Figure 10A,B. In general, the sulfur isotope compositions of different sulfides are consistent and fall within a narrow  $\delta^{34}\text{S}$  range of  $-0.54$  to  $+1.22\text{‰}$  (avg.  $0.44\text{‰}$ ,  $n = 38$ ). The  $\delta^{34}\text{S}$  values of pyrite in stage IVa and stage IVb are  $-0.54 \sim +0.95\text{‰}$  (avg.  $0.24\text{‰}$ ,  $n = 8$ ) and  $0.11 \sim +1.22\text{‰}$  (avg.  $0.65\text{‰}$ ,  $n = 18$ ), respectively; the  $\delta^{34}\text{S}$  values of chalcopyrite in stage IVb range from  $-0.19$  to  $+0.73\text{‰}$  (avg.  $0.26\text{‰}$ ,  $n = 12$ ). The *in-situ* Pb isotopic ratios of pyrite in stage IVb are presented in Supplementary Table S4, Supplementary Figure S2 and Figure 10C,D, and the  $^{206}\text{Pb}/^{204}\text{Pb}$ ,  $^{207}\text{Pb}/^{204}\text{Pb}$  and  $^{208}\text{Pb}/^{204}\text{Pb}$  ratios are 17.323–17.383, 15.424–15.452 and 37.367–37.454, respectively ( $n = 12$ ).

## 6 Discussion

### 6.1 Element behavior during the skarn formation process

#### 6.1.1 Magnetite

There are weak positive correlations between Al (Mg, Na) and Si in magnetite (Supplementary Figure S1), which may indicate the absence of sub-micro-scale silicate inclusions in magnetite (Bowles et al., 2011; Xie et al., 2017), consistent with their flat depth profiles (Figure 13A). Considering magnetite with pervasive micro-porosities is wrapped in metal sulfide (Figure 6H), magnetite in Tongjing deposit was interpreted as a hydrothermal overprint that may have

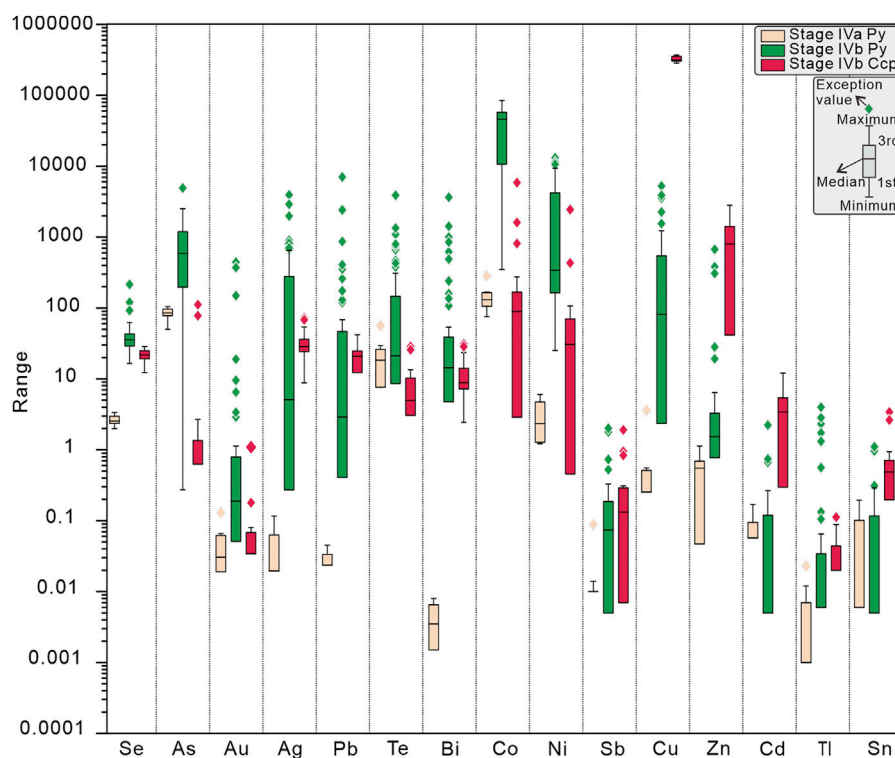


**FIGURE 9**

Trace element distribution diagram showing the variation in the Se, As, Au, Ag, Pb, Te, Bi, Co, Ni, Sb, Cu, Zn, Cd, Tl, and Sn concentrations (in ppm) for pyrite and chalcopyrite.

leached Mg, Si, Al and Ca during the dissolution–reprecipitation process (Hu et al., 2014). Positive correlations exist for Sn vs W, Pb vs W and Sn vs Pb (Figure 11A–C) showing that these elements behave similarly during the skarn formation process. A correlation between Al and Ga (Figure 11D) indicates similar geochemical behaviors (Huang et al., 2016). The contents of Co, Ni, Mo, Cu, Zn and Pb in magnetite would be affected by sulfides because these elements can partition into magnetite and sulfide phases in sulfide-bearing magmatic and hydrothermal systems (Huang et al., 2016). Pyrrhotite and pentlandite do not occur in the Tongjing deposit, so Ni tends to partitioned into magnetite (Dare et al., 2012), with a high content of Ni (39–369 ppm; avg. 182.2 ppm; n = 9) in magnetite. The low Co content of magnetite in the Tongjing and a positive correlation of Cu vs Co (Figure 11E) imply the increasing amounts of sulfides during the skarn formation (Huang et al., 2014; Zhao and Zhou, 2015), consistent with the fact that magnetite is wrapped by pyrite (Figure 6H).

### 6.1.2 Sulfide (pyrite and chalcopyrite)

Although the As content of pyrite in stage IVa is lower than in stage IVb, all points plot well below the solubility saturation line on the Au–As discrimination diagram

(Figure 12) proposed by Reich et al. (2005), suggesting that  $\text{Au}^+$  is the dominant form of Au within the pyrite crystal lattice and that gold-bearing ore fluids deposited this sulfide were largely undersaturated (Reich et al., 2013). Arsenic is relatively rich in pyrite, generally greater than 20 ppm. A positive correlation exists between As and Au (Figure 12A) as described by numerous scholars (Mumin et al., 1994; Reich et al., 2005; Deditius et al., 2014), which is related to the preferential precipitation of Au in the As-rich sulfides (Voute et al., 2019). The above positive correlation indicates As could enter the pyrite lattice through coupled substitution with Au ( $\text{Au}^+ + \text{As}^{3+} \leftrightarrow 2\text{Fe}^{2+}$ ; Deditius et al., 2008), illustrated by the fact that As has a flat depth profile (Figures 13C,D) and the negative correlation between As and Fe (Figure 12B).

The Co and Ni contents of pyrite in stage IVb are higher than those in stage IVa and they have nearly flat depth profiles (Figures 13B–E). The atomic radius and ionic charge of Co and Ni are very close to  $\text{Fe}^{2+}$  (Vaughan and Rosso, 2006; George et al., 2018b), indicating that Co and Ni were lattice-bound or homogeneously distributed as nanoparticles in the pyrite crystals (e.g., Zhang et al., 2022). Almost all pyrite are below the Au solubility line

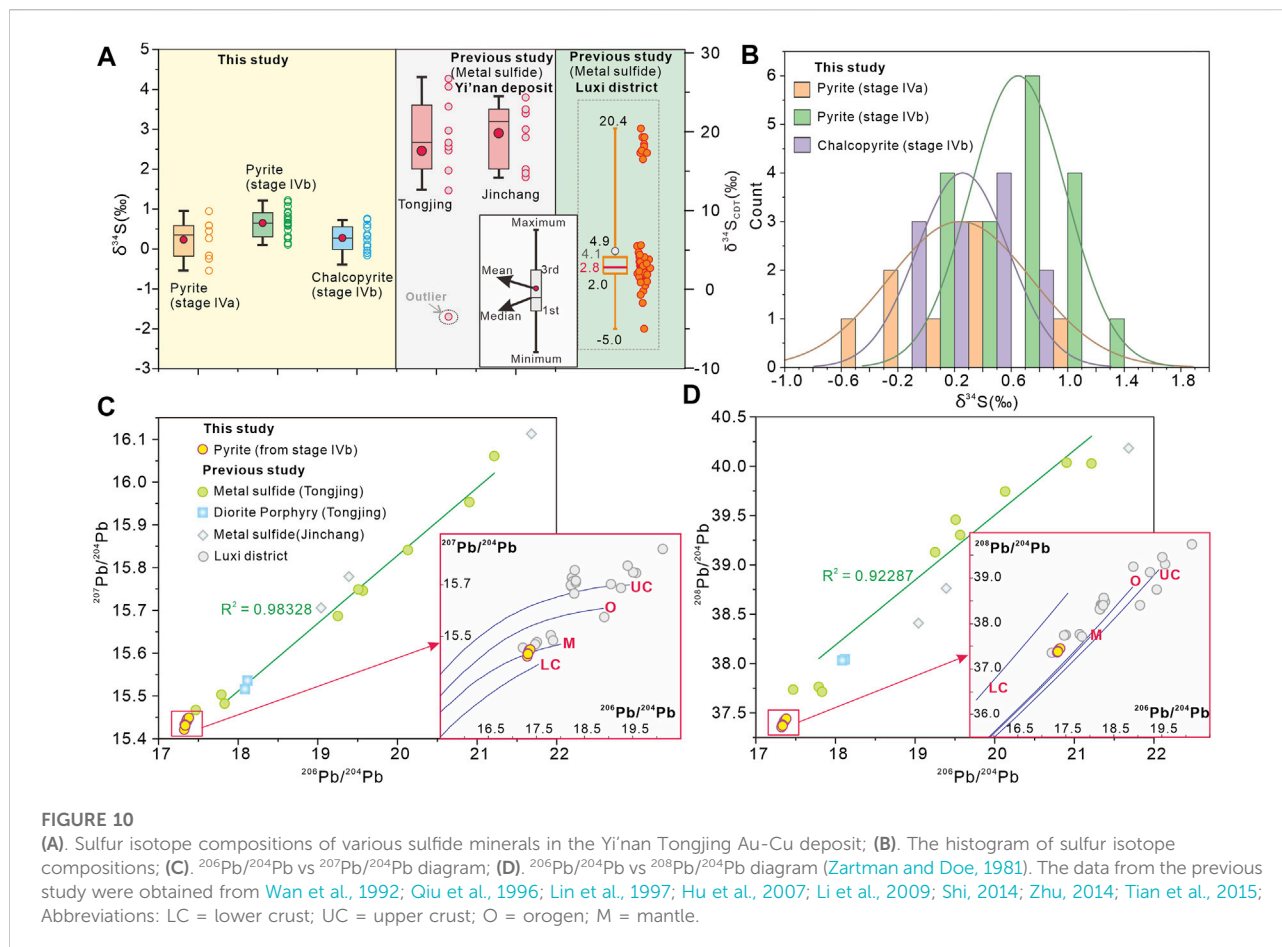


(Figure 12A) but above the Te solubility line (Figure 12C), despite the fact that the Te content of pyrite in stage IVb is higher than stage IVa. Hence, potential telluride inclusions may be characterized by high Te/Au ratios either due to high Te content or high abundances of other elements, such as Cu, Ag, Pb and Bi (e.g., high-sulfidation epithermal pyrite; Naden and Henney, 1995; Berger et al., 2014). Tellurium of pyrite in stage IV is positively correlated with Bi ( $R^2 = 0.57$ , Figure 12D) but also with Ag ( $R^2 = 0.79$ , Figure 12E), which may be related to the occurrence of Bi-Te or Ag-Te mineral inclusions. The identification of the hessite ( $\text{Ag}_2\text{Te}$ ), cervelleite ( $\text{Ag}_4\text{TeS}$ ) and tetradymite ( $\text{Bi}_2\text{Te}_2\text{S}$ ) by microscopic observation (Figures 6I,J; Supplementary Figure S1F) and their similar peaks and irregular depth profiles (Figures 13B–D) prove the above conclusion. It is also worth noting that the concentrations of Ag, Bi and Pb are highly variable in pyrite and chalcopyrite (Supplementary Table S2), and they are significantly positively correlated (Figures 12F,G). The ionic radius of Ag, Pb and Bi are quite different from those of Cu and Fe (Wang et al., 2021), thus they cannot enter the lattice of chalcopyrite or pyrite in the form of a solid solution.

Furthermore, they have similar peaks and irregular depth profiles (Figure 13E), probably due to the micron-scale inclusions of matildite ( $\text{AgBiS}_2$ ), galenobismutite ( $\text{PbBi}_2\text{S}_4$ ) and gustavite ( $\text{AgPbBi}_3\text{S}_6$ ) or bismuth-bearing galena (Maslennikov et al., 2009). Almost all pyrite, chalcopyrite and sphalerite samples show elevated Bi content (>1 ppm) (Figure 12H), which probably reflects the contribution of sedimentation to the hydrothermal system (Koski et al., 1988; Zierenberg et al., 1993). This is consistent with the fact that Proterozoic to Cambrian carbonate sequences was involved during the formation of the Tongjing skarn deposit.

Given the high contents of Co (350–84521 ppm) and Ni (25–13117 ppm) in stage IVb pyrite, the high Co and Ni contents in stage IVb chalcopyrite may be due to the inheritance of the replaced pyrite in stage IVb (Figure 6H; e.g., the Yaman-Kasy volcanic-hosted massive sulfide deposit; Maslennikov et al., 2009). The contents of As, Co and Ni in chalcopyrite vary greatly (Supplementary Table S2) and generally show a similar peak on the depth profiles (Figures 13F,G), suggesting the existence of inclusions, for example siegenite ( $\text{CoNi}_2\text{S}_4$ ). The high Zn content in chalcopyrite (mostly >100 ppm) may be attributed to the

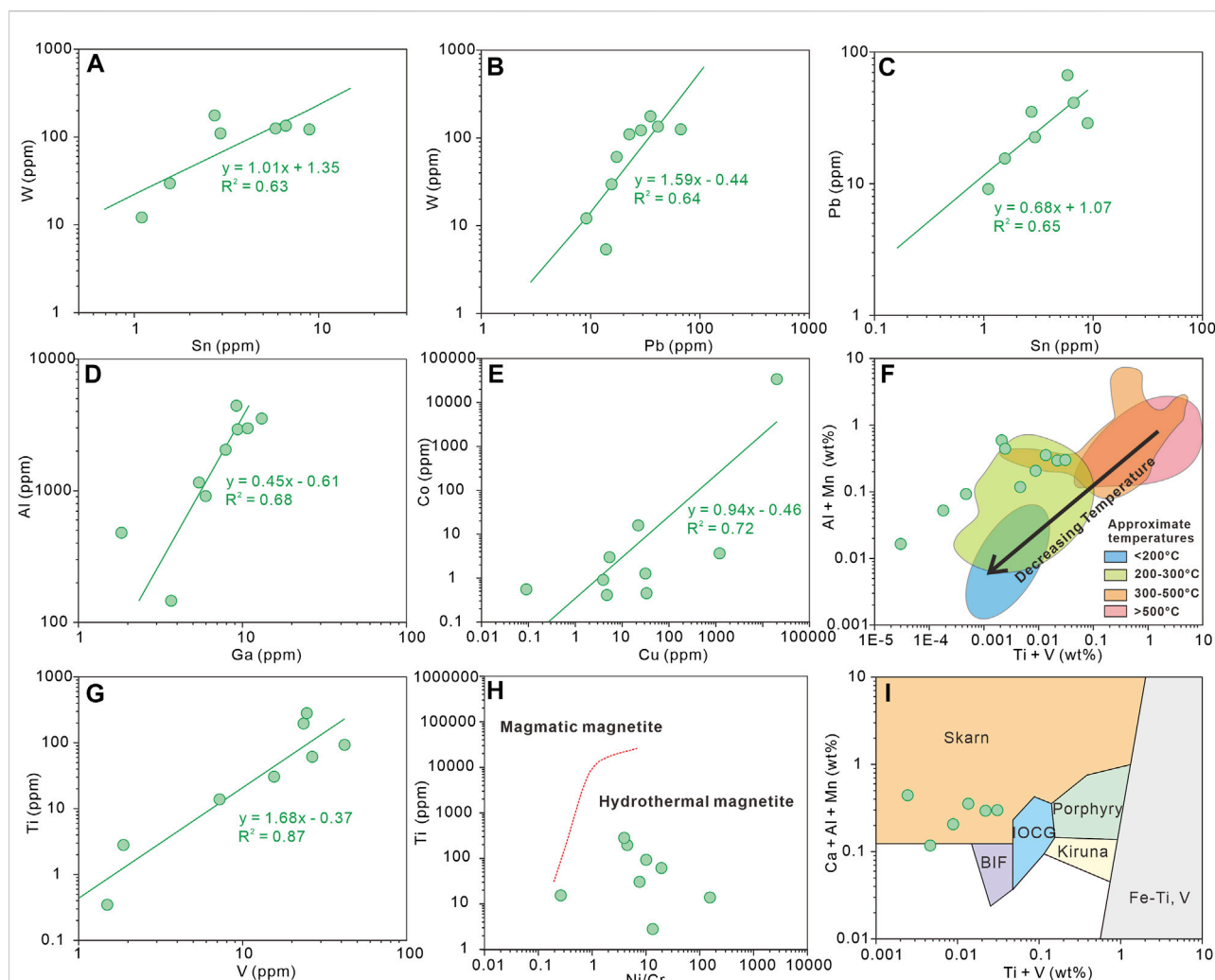


**FIGURE 11**

Correlation diagrams of various trace elements (in ppm) in the studied magnetite from the Yi'nan Tongjing Au–Cu deposit. (A) Sn vs W; (B) Pb vs W; (C) Sn vs Pb; (D) Ga vs Al; (E) Cu vs Co; (F) The Ti + V vs Al + Mn plots displays are clear decreasing temperature trend. Note that those temperatures are estimates based on published values (Ahmad and Rose, 1980; Beane and Tittley, 1981; Leach et al., 1988; Hayes, 1990; Landis and Hofstra, 1991; Doughty and Chamberlain, 1996; Manske and Paul, 2002; Audetat and Pettke, 2006; Thorne et al., 2008; Sillitoe, 2010; Nadoll et al., 2012); (G) V vs Ti; (H) Ni/Cr vs Ti; (I) Ti + V vs Ca + Al + Mn (Dupuis and Beaudoin, 2011). Abbreviations: BIF–Banded iron formation, IOCG–Iron oxide–copper–gold deposits, PCDs–Porphyry Cu deposits, Kiruna–Kiruna apatite–magnetite deposits, Fe–Ti, V–Magmatic Fe–Ti–oxide deposits.

inclusion of sphalerite or zinc-bearing minerals (e.g., Song et al., 2019). Furthermore, the Zn vs Cd diagram (Figure 12I) shows a positive correlation between the two elements in chalcopyrite, and they share the same irregular depth profiles (Figure 13H). This also suggests that the Zn content reflects the proportion of sphalerite inclusions. In addition, the multi-peaked curve of Zn on the depth profiles (Figures 13F–H) implies the presence of zinc-bearing minerals inclusions in chalcopyrite. Chalcopyrite samples with high Ag/As ratios plotting outside of the triangular wedge-shaped zone (Figure 12J) may suggest the presence of silver-bearing inclusions, as supported by a positive correlation between Pb and Ag (Figure 12F).

## 6.2 Possible factors controlling the composition of magnetite and sulfides

It is well known that oxygen fugacity ( $f_{\text{O}_2}$ ) is a major factor that governs element behavior and possibly influenced Au speciation during the ore-forming process (e.g., Keith et al., 2014; Ma et al., 2022). The content of V in magnetite can be used to estimate the relative oxygen fugacity during the ore-forming process (Nadoll et al., 2014, 2015; Canil et al., 2016), and increasing oxygen fugacity would decrease the V content in magnetite by converting  $\text{V}^{3+}$  to  $\text{V}^{4+}$  or  $\text{V}^{5+}$  (Takeno, 2005; Papike et al., 2015). The low V content in magnetite varies from 1.50 ppm to 41.87 ppm (avg. 18.06 ppm), implying a

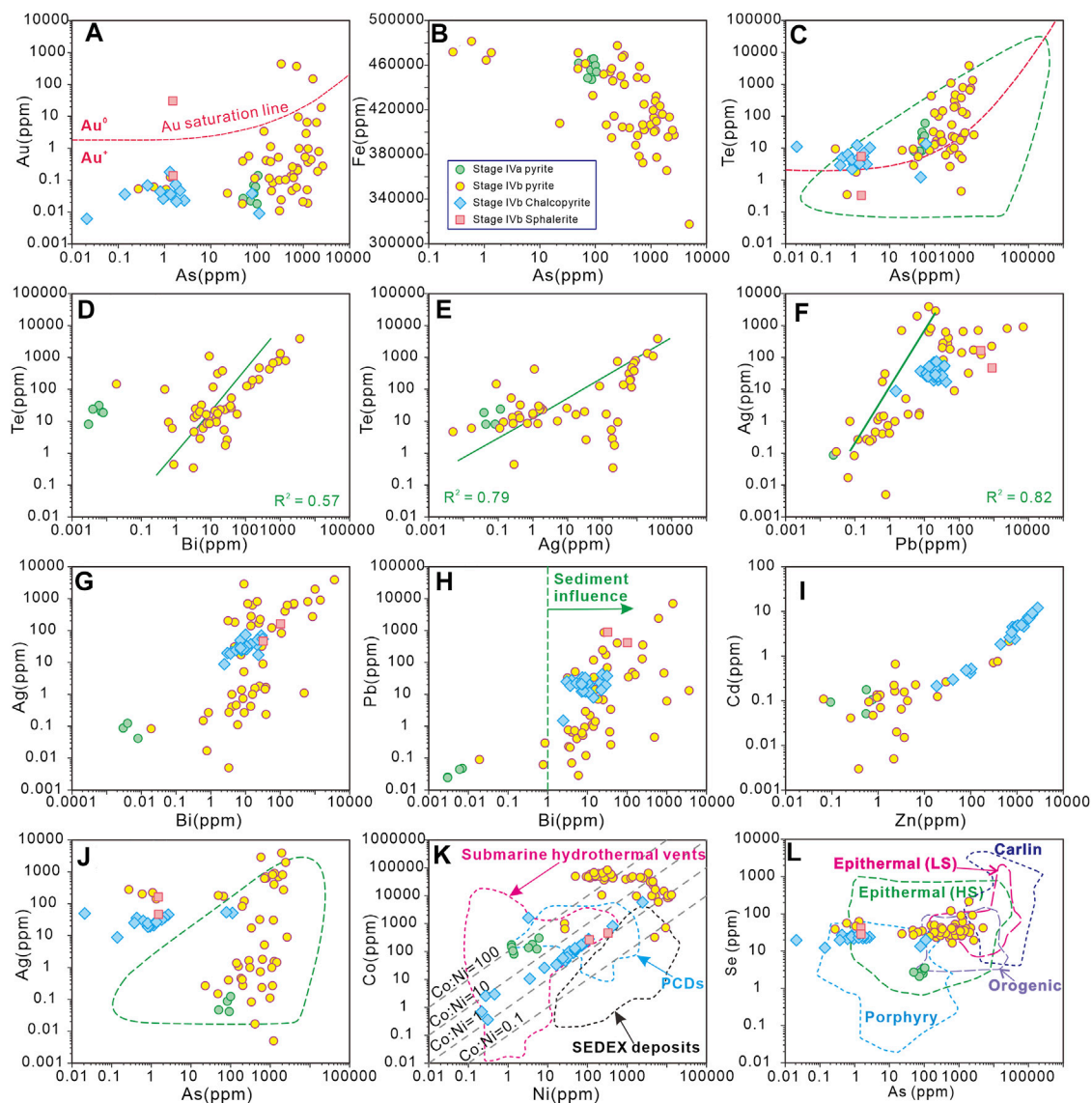


**FIGURE 12**

Plots of various trace elements in the studied pyrite from the Yi'nan Tongjing Au–Cu deposit. (A) Au vs As (Gold saturation line is from Reich et al., 2005); (B) As vs Fe; (C) As vs Te (The green dashed line defines the wedge-shaped zone indicating Te solid solution in pyrite. The red dashed line defines the solubility limit for Te solid solution in pyrite as a function of As, which is based on the equation presented by Reich et al. (2005) for the Au–As system.); (D) Bi vs Te; (E) Ag vs Te; (F) Pb vs Ag; (G) Bi vs Ag; (H) Bi vs Pb (after Keith et al., 2016); (I) Zn vs Cd; (J) As vs Ag (The green dashed line defines the wedge-shaped zone indicating Ag solid solution for pyrites; Reich et al., 2005); (K) Ni vs Co (Deditius et al., 2013; Cioacă et al., 2014; Keith et al., 2016); (L) As vs Se (Gadd et al., 2016; Mukherjee and Large, 2017; Keith et al., 2018 and references therein).

high oxygen fugacity. Temperature is considered another major governing factor for the composition of hydrothermal magnetite, and Ti is a good temperature indicator (Nadoll et al., 2014). There is a visible temperature trend in the data. Figure 11F shows a Ti + V vs Al + Mn plot where data points have been attributed with approximate temperatures—from low temperature (Thorne et al., 2008), intermediate temperature to high temperature (e.g., Manske and Paul, 2002; Sillitoe, 2010). The magnetite grains mainly fall in the overlapping area of medium temperature

(200–300°C) and high temperature (300–500°C), higher than the formation temperature of pyrite (see below).

Selenium in pyrite can be used as a proxy for relative temperature estimations in ore-forming fluids (Huston et al., 1995; Keith et al., 2018). Selenium can substitute for S in pyrite (Chouinard et al., 2005), and its concentration increases as fluid temperature decreases (Keith et al., 2018). Selenium is nearly completely removed from the fluid at temperatures above 300°C (Huston et al., 1995). Compared with the Se content

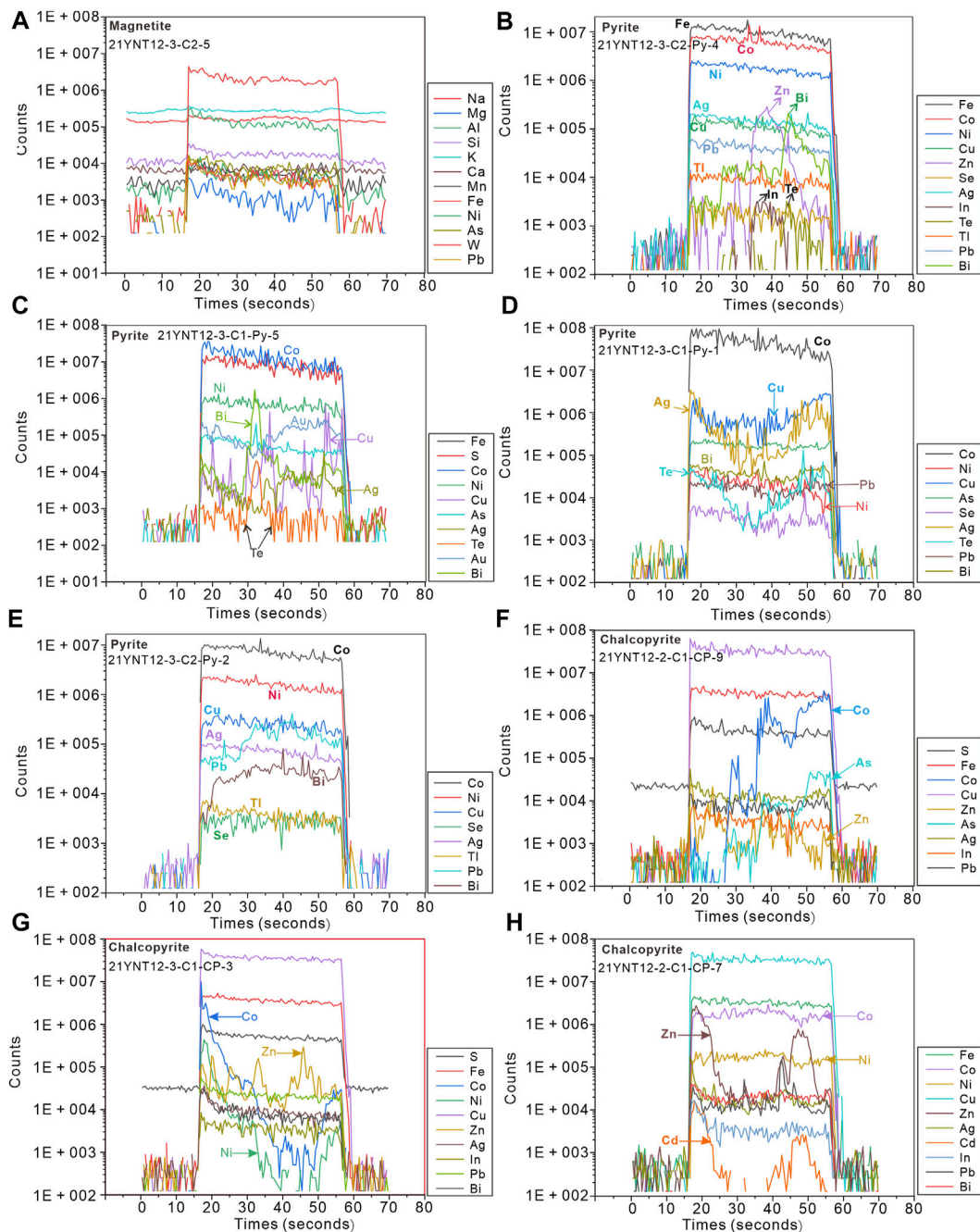


**FIGURE 13**

Representative time-resolved LA-ICP-MS depth profiles for magnetite (A), pyrite (B–E) and chalcoprite (F–H).

(16.49–214.74 ppm) of pyrite in stage IVb, the Se content of pyrite in stage IVa is low, distributed between 1.99 and 3.36 ppm. It indicates that the temperature of ore-forming fluids in the Tongjing deposit is not high (<300 °C), consistent with previous studies (190–250 °C; Dong, 2008), but it cannot be excluded from the genetic relationship with magmatic activities. The Se content of pyrite may vary with the pH and redox conditions of the ore-forming fluid (Keith et al., 2018).

The low Se (<10 ppm) and (As < 100 ppm) contents of pyrite are consistent with the Se (avg. 2.64 ppm) and As (avg. 84.20 ppm) contents of pyrite from stage IVa, indicating that the ore-forming fluid is characterized by high temperatures, high  $f_{O_2}$ , moderate to high salinity and acidic pH, for example porphyry deposit (Figure 12L; Goldfarb et al., 2005). The high Se (>10 ppm) and As (>100 ppm) contents of pyrite are consistent with the Se (avg.

43.26 ppm) and As (avg. 842 ppm) contents of pyrite from Stage IVb, suggesting that the ore-forming fluids were distinguished by low temperatures, low  $f_{O_2}$ , low salinity and near-neutral pH, as in orogenic and epithermal (LS) deposits (Figure 12I; Goldfarb et al., 2005; Simmons et al., 2005). Thus, as ore-forming fluid evolves, the temperature, salinity and  $f_{O_2}$  of the ore-forming fluid decrease and the pH rises, resulting in the unloading of Au. Furthermore, pyrite and telluride precipitation in the Tongjing deposit was caused by a decrease in  $f_{O_2}$  but pH-independent (Cooke and McPhail, 2001; Grundler et al., 2013; Keith et al., 2018), which is similar to the Dongping Au deposit (Cook et al., 2009; Gao et al., 2017).

### 6.3 Source of ore-forming materials

The sulfur isotope composition of hydrothermal minerals depends on the total sulfur isotope composition,  $f_{O_2}$ , pH and temperature of the fluid (Ohmoto, 1972). At Tongjing, pyrite has higher  $\delta^{34}S$  values (avg. 0.52‰; Supplementary Table S3; Figures 10A,B) than chalcopyrite (avg. 0.26‰), indicating that the ore-forming system is in equilibrium for sulfur isotope fractionation (Chen et al., 2008). Thus, the total sulfur isotope value of hydrothermal fluids can be used to indicate the source of ore-forming material (Chen et al., 2008). The  $\delta^{34}S_{\text{Sulfide-H}_2\text{S}}$  of pyrite at 200°C and 250°C are 0.1‰ and -0.3‰ respectively (Kajiwara and Krouse, 1971). Previous microthermometric measurements of fluid inclusions (Dong, 2008) and this study of Se content in pyrite indicated that the ore-forming temperatures of stages IVa and IVb are approximately 200°C and 250°C, respectively. According to the formula ( $\delta^{34}S_{\Sigma S} = \delta^{34}S_{\text{Sulfide}} - \delta^{34}S_{\text{Sulfide-H}_2\text{S}}$ ; Ohmoto, 1972), the  $\delta^{34}S_{\Sigma S}$  values were calculated to be 0.14‰ and 0.95‰ (Supplementary Table S3) for stages IVa and IVb, respectively. This narrow variation is comparable to magmatic origin ( $\delta^{34}S = 0 \pm 3\%$ ; Ohmoto and Rye, 1979; Chaussidon and Lorand, 1990). Combined with previous bulk-sulfur isotope analyses (Figure 10A), high  $\delta^{34}S$  values (up to 5‰) do not exclude a small contribution from wall rocks (sedimentary or metamorphic rocks). Such a sulfur isotopic composition, consistent with the sulfur isotope composition of the other gold deposits in the Luxi district (Figure 10A), is common in skarn-type deposits (e.g., Shu et al., 2013; Peng et al., 2016; Cai et al., 2021).

Lead isotope composition can be used to infer the source of Pb, and thus the ore-forming materials. The Pb isotope data in this study show a strong linear relationship with the previous data obtained by bulk analyses (sulfides and diorite porphyry) (Figures 10C,D), implying that diorite porphyry is a key source of ore-forming material for mineralization. The *in-situ* Pb isotope data are more concentrated ( $^{206}\text{Pb}/^{204}\text{Pb} = 17.323\text{--}17.383$ ;  $^{207}\text{Pb}/^{204}\text{Pb} = 15.424\text{--}15.452$ ;  $^{208}\text{Pb}/^{204}\text{Pb} = 37.367\text{--}37.454$ ), indicating a uniform source. In the  $^{206}\text{Pb}/^{204}\text{Pb}$  vs  $^{207}\text{Pb}/^{204}\text{Pb}$  diagram, the Pb isotope data of pyrite from the Tongjing deposit fall near the mantle evolution curve (Figure 10C); the data are close to the mantle/orogen and lower crust curves in the  $^{206}\text{Pb}/^{204}\text{Pb}$  vs  $^{208}\text{Pb}/^{204}\text{Pb}$  diagrams (Figure 10D). This implies that diorite porphyry (major) and marble/limestone are

the source of the ore-forming materials, consistent with what is suggested by the sulfur isotope composition.

### 6.4 Ore genesis of Tongjing Au-Cu deposit

Magnetite shows a positive correlation between V and Ti (Figure 11G), and the behavior of Ni and Cr in magnetite is decoupled (Ni/Cr ratios  $\geq 1$ ; Figure 11H; Dare et al., 2014), indicating a hydrothermal magnetite origin (e.g., Huang et al., 2016). Magnetite is Ca-depleted (below detection limit) and has low REE contents (1.66–12.15ppm; avg. 4.87ppm), consistent with the characteristics of hydrothermal magnetite (Knipping et al., 2015). Furthermore, the plot of Ca + Al + Mn vs Ti + V (Figure 11I; Dupuis and Beaudoin, 2011) can distinguish magnetite from various origins. For the Tongjing deposit, the data of magnetite plot into the skarn field, though a small number of grains plot in the undefined field due to lower Ca + Al + Mn contents (Figure 11I).

Cobalt and Ni contents of pyrite can reflect the temperature and origin of pyrite (Bralia et al., 1979; Campbell and Ethier, 1984; Bajwah et al., 1987; Gregory et al., 2015). Cobalt prefers to enter pyrite at high temperatures, while Ni prefers to enter pyrite at low temperatures (Maslennikov et al., 2009; Zhang et al., 2020). The Co/Ni ratios of pyrite from Tongjing vary widely, ranging from 0.07 to 1,009 (Figure 12K). Most values are greater than 10, suggesting that pyrite was formed at a high temperature and originated from hydrothermal/magmatic (Bralia et al., 1979; Bajwah et al., 1987; Meng et al., 2018). Low Co/Ni ratios (generally  $< 1$ ; Figure 12K) are suggested to represent pyrite of syn-sedimentary origin (Koglin et al., 2010; Large et al., 2014). A few Co/Ni ratios are between 0.01 and 1, indicating the mixing of carbonate rocks during mineralization. The variable Co and Ni contents of the studied pyrite are mainly plotted in or outside the porphyry copper deposit area (away from the submarine hydrothermal vents and SEDEX deposits areas) (Figure 12K), also indicating the result of magmatic–hydrothermal processes. Chalcopyrite and pyrite have low U and V contents (Supplementary Table S2), indicating that they precipitated in the hydrothermal fluids.

Deditius et al. (2009) and Tardani et al. (2017) pointed out that processes such as fluid boiling can fractionate trace elements in hydrothermal fluids causing systematic compositional differences and chemical zonation in precipitated pyrite. Results of Loftus-Hill and Solomon (1967) and Schirmer et al. (2014) highlighted that oceanic sediments and carbonate-bearing rocks are enriched in Te compared to other rocks. As the ore-forming intrusion of the Tongjing Au-Cu deposit, the formation of the Tongjing pluton is related to the mantle metasomatism by the paleo-Pacific plate (Guo et al., 2014). The Cambrian sequences are the main wall rock of the Tongjing Au-Cu deposit, mainly including carbonate rocks such as limestone and dolomite (Figure 4A; Dong, 2008). We conclude that the Te of pyrite from the Tongjing deposit may be controlled by its concentration in the source rocks, which is also supported by the

occurrence of the nearby Mesozoic Guilaizhuang Au (-Te) deposit (Yu et al., 2019).

During the Late Mesozoic, the NCC underwent significant decratonization and massive thinning of the lithospheric mantle, accompanied by huge upwelling of the asthenosphere due to the roll-back of the paleo-Pacific plate (Zhu et al., 2011; Li et al., 2020; Yang et al., 2021). The response to this tectonic event in the eastern part of the NCC is mainly characterized by large-scale gold mineralization in the Jiaodong and Luxi districts. The highly concentrated sulfur and lead isotope values/ratios in this study indicate that deep magma (probable mantle) source of ore-forming materials. That is the Tongjing diorite porphyry enriched in ore-forming elements intruded into limestone and formed a large number of skarn and Cu–Au ore bodies.

## Conclusion

- 1) Five hydrothermal stages are identified in the Yi'nan Tongjing Au-Cu deposit: 1) early skarn; 2) late skarn; 3) oxide; 4) sulfide; and 5) late quartz–calcite.
- 2) Gold occurs mainly as (silver-bearing) native grains. The trace element composition of the sulfides and oxides implies that the original ore-forming fluid is of medium-high temperature magmatic-hydrothermal origin. The decrease in temperature, salinity and  $f_{O_2}$  of the ore-forming fluid, and the increased pH of the ore-forming fluid are critical to the precipitation of ore minerals.
- 3) *In-situ* LA-ICP-MS sulfur and lead isotope compositions indicate that the origin of ore-forming materials comes from the Early Cretaceous diorite porphyry and partly from the host rocks (carbonate rocks).
- 4) The present study provides new constraints for the mineralization process of skarn deposits in the Luxi district.

## Data availability statement

The original contributions presented in the study are included in the article/Supplementary Material, further inquiries can be directed to the corresponding author.

## Author contributions

Conceptualization, W-YC and Z-LZ; methodology, W-YC and XL; validation, J-LG, MM and Y-DL; formal analysis and data curation, Y-XS and Z-SL; project administration, W-YC and Z-LZ; writing—original draft, W-YC. All authors have read and agreed to the published version of the manuscript.

## Funding

This study was financially supported by the Natural Science Foundation of Shandong Province (no. ZR2021QD056 and ZR2021QD106), Open Project Fund of Key Laboratory of Gold Mineralization Processes and Resource Utilization, MNR (no. Kfkt202108 and Kfkt202124) and Early Cretaceous Magmatism and Metallogensis in TYD-ZS Fault (no. KC202005 and KC202102).

## Acknowledgments

We are grateful to Xiangbiao-Sun and Bingbing-Liu from the Yi'nan Gold Mine of Shandong Gold Group and Associate Professors Yongming-Zhang and Liping-Liu of Shandong University of Technology for their help and support during the fieldwork.

## Conflict of interest

The authors declare that the research was conducted in the absence of any commercial or financial relationships that could be construed as a potential conflict of interest.

The reviewer QS declared a shared affiliation with the author WC to the handling editor at time of review.

## Publisher's note

All claims expressed in this article are solely those of the authors and do not necessarily represent those of their affiliated organizations, or those of the publisher, the editors and the reviewers. Any product that may be evaluated in this article, or claim that may be made by its manufacturer, is not guaranteed or endorsed by the publisher.

## Supplementary material

The Supplementary Material for this article can be found online at: <https://www.frontiersin.org/articles/10.3389/feart.2022.1084212/full#supplementary-material>

### SUPPLEMENTARY FIGURE S1

BSE and EDS images for native gold and sulfides (A–F); scatter plot of trace elements in magnetite (G–I).

### SUPPLEMENTARY FIGURE S2

Photomicrograph of pyrite in stages IVa (A) and IVb (B,C), including the spots of *in situ* trace element and sulfur-lead isotope analysis.

### SUPPLEMENTARY TABLE S1

Major element composition of magnetite, native gold and sulfides determined by EPMA.

### SUPPLEMENTARY TABLE S2

Trace element composition of magnetite and sulfides determined by LA-ICP-MS.

#### SUPPLEMENTARY TABLE S3

## References

- Ahmad, S. N., and adn Rose, A. W. (1980). Fluid inclusions in porphyry and skarn ore at Santa Rita. *New Mex. Econ. Geol.* 75, 229–250.
- Audetat, A., and Pettek, T. (2006). Evolution of a porphyry-Cu mineralized magma system at Santa Rita, New Mexico (USA). *J. Petrology* 47, 2021–2046. doi:10.1093/petrology/egl035
- Bajwah, Z. U., Seccombe, P. K., and Offler, R. (1987). Trace element distribution Co: Ni ratios and Genesis of the big cadia iron-copper deposit, new south Wales, Australia. *Mineral. Deposita* 22, 292–300. doi:10.1007/bf00204522
- Baker, T., Ebert, S., Rombach, C., and Ryan, C. G. (2006). Chemical compositions of fluid inclusions in intrusion-related gold systems, Alaska and Yukon, using PIXE microanalysis. *Econ. Geol.* 101, 311–327. doi:10.2113/gsecongeo.101.2.311
- Beane, R. E., and Titley, S. R. (1981). Porphyry copper deposits, part II. Hydrothermal alteration and mineralization. *Econ. Geol.*, 235–269. (75th Anniversary).
- Berger, B. R., Henley, R. W., Lowers, H. A., and Pribil, M. J. (2014). The lepanto Cu–Au deposit, Philippines: A fossil hyperacidic volcanic lake complex. *J. Volcanol. Geotherm. Res.* 271, 70–82. doi:10.1016/j.jvolgeores.2013.11.019
- Bowles, J. F. W., Howie, R. A., Vaughan, D. J., and Zussman, J. (2011). *Rock-forming minerals — non-silicates: Oxides, hydroxides and sulphides*. 2nd ed. London: Geological Society.
- Bralia, A., Sabatini, G., and Troja, F. (1979). A revaluation of the Co/Ni ration in pyrite as geochemical tool in ore Genesis problems. *Min. Deposita* 14, 353–374.
- Cai, W. Y., Wang, K. Y., Li, J., Fu, L. J., Li, S. D., Yang, H., et al. (2021). Genesis of the bagenheigeqier Pb–Zn skarn deposit in inner Mongolia, NE China: Constraints from fluid inclusions, isotope systematics and geochronology. *Geol. Mag.* 158, 271–294. doi:10.1017/s0016756820000473
- Campbell, F. A., and Ethier, V. G. (1984). Nickel and cobalt in pyrrhotite and pyrite from the Faro and Sullivan orebodies. *Can. Mineral.* 22, 503–506.
- Canil, D., Grondahl, C., Lacourse, T., and Pisiak, L. K. (2016). Trace elements in magnetite from porphyry Cu–Mo–Au deposits in British Columbia. Canada. *Ore Geol. Rev.* 72, 1116–1128. doi:10.1016/j.oregeorev.2015.10.007
- Chang, Z., Shu, Q., and Meinert, L. D. (2019). *Skarn deposits of China*, 22. Littleton, Colorado: Society of Economic Geologists, Special Publication, 189–234.
- Chaussidon, M., and Lorand, J. P. (1990). Sulphur isotope composition of orogenic spinel lherzolite massifs from Ariège (North-Eastern Pyrenees, France): An ion microprobe study. *Geochimica Cosmochimica Acta* 54, 2835–2846. doi:10.1016/0016-7037(90)90018-g
- Chen, L., Tao, W., Zhao, L., and Zheng, T. (2008). Distinct lateral variation of lithospheric thickness in the Northeastern North China Craton. *Earth Planet. Sci. Lett.* 267, 56–68. doi:10.1016/j.epsl.2007.11.024
- Chen, Y. J., Chen, H. Y., Zaw, K., Pirajno, F., and Zhang, Z. J. (2007). Geodynamic settings and tectonic model of skarn gold deposits in China: An overview. *Ore Geol. Rev.* 31, 139–169. doi:10.1016/j.oregeorev.2005.01.001
- Chinnasamy, S. S., Hazarika, P., Pal, D., Sen, R., and Govindaraj, G. (2021). Pyrite textures and trace element compositions from the granodiorite-hosted gold deposit at jonmagiri, eastern dharwar craton, India: Implications for gold mineralization processes. *Econ. Geol.* 116, 559–579. doi:10.5382/econgeo.4787
- Chouinard, A., Paquette, J., and Williams-Jones, A. E. (2005). Crystallographic controls on trace-element incorporation in auriferous pyrite from the Pascua epithermal high-sulfidation deposit, Chile-Argentina. *Can. Mineralogist* 43, 951–963. doi:10.2113/gscanmin.43.3.951
- Cioacă, M. E., Munteanu, M., Qi, L., and Costin, G. (2014). Trace element concentrations in porphyry copper deposits from metaliferi mountains, Romania: A reconnaissance study. *Ore Geol. Rev.* 63, 22–39. doi:10.1016/j.oregeorev.2014.04.016
- Cook, N. J., Ciobanu, C. L., and Mao, J. (2009). Textural control on gold distribution in as-free pyrite from the dongping, huangtuliang and hougou gold deposits, north China craton (hebei province, China). *Chem. Geol.* 264, 101–121. doi:10.1016/j.chemgeo.2009.02.020
- Cooke, D. R., and McPhail, D. C. (2001). Epithermal Au–Ag–Te mineralization, Acupan, Baguio district, Philippines: Numerical simulations of mineral deposition. *Econ. Geol.* 96, 109–131. doi:10.2113/96.1.109
- Dare, S. A., Barnes, S.-J., Beaudoin, G., Méric, J., Boutroy, E., and Potvin-Doucet, C. (2014). Trace elements in magnetite as petrogenetic indicators. *Min. Deposita* 49, 785–796. doi:10.1007/s00126-014-0529-0
- Dare, S. A. S., Barnes, S. J., and Beaudoin, G. (2012). Variation in trace element content of magnetite crystallized from a fractionating sulfide liquid, Sudbury, Canada: Implications for provenance discrimination. *Geochimica Cosmochimica Acta* 88, 27–50. doi:10.1016/j.gca.2012.04.032
- Deditius, A., Chryssoulis, S., Li, J. W., Ma, C. Q., Parada Reyes, M., Barra, F., et al. (2013). Pyrite as a record of hydrothermal fluid evolution in a porphyry copper system: A SIMS/EMPA trace element study. *Geochimica Cosmochimica Acta* 104, 42–62. doi:10.1016/j.gca.2012.11.006
- Deditius, A. P., Reich, M., Kesler, S. E., Utsunomiya, S., Chryssoulis, S. L., Walshe, J., et al. (2014). The coupled geochemistry of Au and as in pyrite from hydrothermal ore deposits. *Geochimica Cosmochimica Acta* 140, 644–670. doi:10.1016/j.gca.2014.05.045
- Deditius, A. P., Utsunomiya, S., Renock, D., Ewing, R. C., Ramana, C. V., Becker, U., et al. (2008). A proposed new type of arsenian pyrite: Composition, nanostructure and geological significance. *Geochimica Cosmochimica Acta* 72, 2919–2933. doi:10.1016/j.gca.2008.03.014
- Deditius, A., Utsunomiya, S., Ewing, R. C., Chryssoulis, S., Venter, D., and Kesler, S. E. (2009). Decoupled geochemical behavior of as and Cu in hydrothermal systems. *Geology* 37, 707–710. doi:10.1130/g25781a.1
- Deng, J., Wang, C., Bagas, L., Santosh, M., and Yao, E. (2018). Crustal architecture and metallogenesis in the south-eastern North China Craton. *Earth-Science Rev.* 182, 251–272. doi:10.1016/j.earscirev.2018.05.001
- Deng, J., and Wang, Q. F. (2016). Gold mineralization in China: Metallogenic provinces, deposit types and tectonic framework. *Gondwana Res.* 36, 219–274. doi:10.1016/j.gr.2015.10.003
- Dong, S. Y. (2008). Beijing: China University of Geosciences, 60–68. Ph.d. thesis (in Chinese with English abstract). Metallogenesis, metallogenic laws and metallogenetic prediction of the yinan gold deposit, shandong province
- Doughty, P. T., and Chamberlain, K. R. (1996). Salmon River arch revisited: New evidence for 1370 Ma rifting near the end of deposition in the Middle Proterozoic belt basin. *Can. J. Earth Sci.* 33, 1037–1052. doi:10.1139/e96-079
- Duan, Z., Gleeson, S. A., Gao, W. S., Wang, F. Y., and Li, J. W. (2020). Garnet U–Pb dating of the Yinan Au–Cu skarn deposit, Luxi District, North China Craton: Implications for district-wide coeval Au–Cu and Fe skarn mineralization. *Ore Geol. Rev.* 118, 103310. doi:10.1016/j.oregeorev.2020.103310
- Duan, Z., and Li, J. W. (2017). Zircon and titanite U–Pb dating of the Zhangjiawa iron skarn deposit, Luxi district, North China Craton: Implications for a craton-wide iron skarn mineralization. *Ore Geol. Rev.* 89, 309–323. doi:10.1016/j.oregeorev.2017.06.022
- Dupuis, C., and Beaudoin, G. (2011). Discriminant diagrams for iron oxide trace element fingerprinting of mineral deposit types. *Min. Deposita* 46, 319–335. doi:10.1007/s00126-011-0334-y
- Einaiudi, M. T., Meinert, L. D., and Newberry, R. J. (1981). “Skarn deposits,” in *Economic Geology: Seventy-fifth anniversary volume*. Editor B. J. Skinner (Littleton, Colorado: Society of Economic Geologist), 317–391.
- Fougerouse, D., Micklethwaite, S., Ulrich, S., Miller, J., Godel, B., Adams, D. T., et al. (2017). Evidence for two stages of mineralization in West Africa’s largest gold deposit: Obuasi, Ghana. *Econ. Geol.* 112, 3–22. doi:10.2113/econgeo.112.1.3
- Gadd, M. G., Layton-Matthews, D., Peter, J. M., and Paradis, S. J. (2016). The world-class howard’s pass SEDEX Zn–Pb district, selwyn basin, yukon. Part I: Trace element compositions of pyrite record input of hydrothermal, diagenetic, and metamorphic fluids to mineralization. *Min. Deposita* 51, 319–342. doi:10.1007/s00126-015-0611-2
- Gao, M. B., Gao, J. L., Zhang, Y. M., Zhang, Z. L., Liu, L. P., Zhang, Y. D., et al. (2022). Magma source and genesis of the kuangshan complex in Laiwu county of the western shandong: Constraints from geochronology, geochemistry, bulk rock Sr–Nd–Pb isotopes and zircon Hf isotopes. *Bull. Mineralogy, Petrology Geochem.*, 1–20. (in Chinese with English abstract).
- Gao, S., Xu, H., Li, S. X., Santosh, M., Zhang, D., Yang, L., et al. (2017). Hydrothermal alteration and ore-forming fluids associated with gold-tellurium

- mineralization in the Dongping gold deposit, China. *Ore Geol. Rev.* 80, 166–184. doi:10.1016/j.oregeorev.2016.06.023
- George, L. L., Cook, N. J., Crowe, B. B. P., and Ciobanu, C. L. (2018a). Trace elements in hydrothermal chalcopyrite. *Mineral. Mag.* 82, 59–88. doi:10.1180/minmag.2017.081.021
- George, L. L., Cristian, B., Massimo, D., and Cook, N. J. (2018b). Textural and trace element evolution of pyrite during greenschist facies metamorphic recrystallization in the southern apuan alps (tuscany, Italy): Influence on the formation of Ti-rich sulfosalt melt. *Ore Geol. Rev.* 102, 59–105. doi:10.1016/j.oregeorev.2018.08.032
- Goldfarb, R. J., Baker, T., Dube, B., Groves, D. I., Hart, C. J., and Gosselin, P. (2005). Distribution, character, and Genesis of gold deposits in metamorphic terranes. *Econ. Geol.* 100, 407–450.
- Goldfarb, R. J., and Groves, D. I. (2015). Orogenic gold: Common or evolving fluid and metal sources through time. *Lithos* 233, 2–26. doi:10.1016/j.lithos.2015.07.011
- Gregory, D. D., Large, R. R., Halpin, J. A., Baturina, E. L., Lyons, T. W., Wu, S., et al. (2015). Trace element content of sedimentary pyrite in Black Shales. *Econ. Geol.* 110, 1389–1410. doi:10.2113/econgeo.110.6.1389
- Groves, D. I., Goldfarb, R. J., Gebre-Mariam, M., and Robert, F. (1998). Orogenic gold deposits: A proposed classification in the context of their crustal distribution and relationship to other gold deposit types. *Ore Geol. Rev.* 13, 7–27. doi:10.1016/s0169-1368(97)00012-7
- Grunder, P. V., Brugger, J., Etschmann, B. E., Helm, L., Liu, W. H., Spry, P. G., et al. (2013). Speciation of aqueous tellurium(IV) in hydrothermal solutions and vapors, and the role of oxidized tellurium species in Te transport and gold deposition. *Geochimica Cosmochimica Acta* 120, 298–325. doi:10.1016/j.gca.2013.06.009
- Gu, X. X., Dong, S. Y., Wang, Y. X., Hu, G. Z., Du, S. H., and Jiao, P. (2008). A new example of unconformity-related endogenic metallization: The Yinan Au-Cu-Fe deposit in Shandong Province, China. *Geoscience* 22, 151–161. (in Chinese with English abstract).
- Guo, P., Santosh, M., Li, S. R., and Li, Q. (2014). Crustal evolution in the central part of Eastern NCC: Zircon U-Pb ages from multiple magmatic pulses in the Luxi area and implications for gold mineralization. *Ore Geol. Rev.* 60, 126–145. doi:10.1016/j.oregeorev.2014.01.002
- Hastie, E. C. G., Kontak, D. J., and Lafrance, B. (2020). Gold remobilization: Insights from gold deposits in the archaean swayze greenstone belt, abitibi subprovince, Canada. *Econ. Geol.* 115, 241–277. doi:10.5382/econgeo.4709
- Hayes, T. S. (1990). A preliminary study of thermometry and metal sources of the Spar Lake stratabound copper-silver deposit, Belt Supergroup, Montana. *U.S. Geol. Surv. Open-File Rep.* 90–48430.
- Hedenquist, J. W., and Lowenstern, J. B. (1994). The role of magmas in the formation of hydrothermal ore deposits. *Nature* 370, 519–527. doi:10.1038/370519a0
- J. W. Hedenquist, J. F. H. Thompson, R. J. Goldfarb, and J. P. Richards (Editors) (2005). *Economic Geology 100th anniversary* (Littleton, Colorado: Society of Economic Geologists, Inc.), 1133.
- Hough, R. M., Butt, C. R., and Fischer-Bühner, J. (2009). The crystallography, metallography and composition of gold. *Elements* 5, 297–302. doi:10.2113/gselements.5.5.297
- Hu, F. F., Wang, Y., Fan, H. R., Zheng, X. L., and Jiao, P. (2010). Geochronology and ore-forming fluids in the jinchang skarn goldcopper deposit, yinan county, Western shandong province. *Acta Petrol. Sin.* 26, 1503–1511. (in Chinese with English abstract).
- Hu, H. B., Mao, J. W., Niu, S. Y., Li, Y. F., and Li, M. W. (2006). Geology and geochemistry of telluridebearing Au deposits in the Pingyi area, Western Shandong, China. *Mineralogy Petrology* 87, 209–240. doi:10.1007/s00710-006-0126-8
- Hu, H. B., Sun, A. Q., Niu, S. Y., Wang, B. D., and Li, Y. P. (2007). Helium and argon isotopic compositions of the Longquanzhan gold deposit in the Yishu fault zone and their geological implications. *Chin. J. Geochem.* 26, 46–51. (in Chinese with English abstract). doi:10.1007/s11631-007-0046-2
- Hu, H., Li, J. W., Lentz, D., Ren, Z., Zhao, X. F., Deng, X. D., et al. (2014). Dissolution-precipitation process of magnetite from the Chengchao iron deposit: Insights into ore Genesis and implication for *in-situ* chemical analysis of magnetite. *Ore Geol. Rev.* 57, 393–405. doi:10.1016/j.oregeorev.2013.07.008
- Hu, Z. C., Zhang, W., Liu, Y. S., Gao, S., Li, M., Zong, K. Q., et al. (2015). Wave<sup>2</sup> signal-smoothing and mercury-removing device for laser ablation quadrupole and multiple collector ICPMS analysis: Application to lead isotope analysis. *Anal. Chem.* 87, 1152–1157. doi:10.1021/ac503749k
- Huang, X., Gao, J., Qi, L., Meng, Y., Wang, Y., and Dai, Z. (2016). *In-situ* LA-ICP-MS trace elements analysis of magnetite: The Fenghuangshan Cu-Fe-Au deposit, Tongling, Eastern China. *Ore Geol. Rev.* 72, 746–759. doi:10.1016/j.oregeorev.2015.09.012
- Huang, X., Qi, L., and Meng, Y. (2014). Trace element geochemistry of magnetite from the Fe(-Cu) deposits in the hami region, eastern tianshan orogenic belt, NW China. *Acta Geol. Sin. - Engl. Ed.* 88, 176–195. (English Edition). doi:10.1111/1755-6724.12190
- Huston, D. L., Sie, S. H., Suter, G. F., Cooke, D. R., and Both, R. A. (1995). Trace elements in sulfide minerals from eastern Australian volcanic-hosted massive sulfide deposits: Part I. Proton microprobe analyses of pyrite, chalcopyrite and sphalerite, and Part II. Selenium levels in pyrite: Comparison with  $\delta^{34}\text{S}$  values and implications for the source of sulfur in volcanogenic hydrothermal systems. *Econ. Geol.* 90, 1167–1196. doi:10.2113/econgeo.90.5.1167
- Keith, M., Haase, K. M., Klemm, R., Krumm, S., and Strauss, H. (2016). Systematic variations of trace element and sulfur isotope compositions in pyrite with stratigraphic depth in the Skouriotissa volcanic-hosted massive sulfide deposit, Troodos ophiolite, Cyprus. *Chem. Geol.* 423, 7–18. doi:10.1016/j.chemgeo.2015.12.012
- Keith, M., Haase, K. M., Schampera, U. S., Klemm, R., Petersen, S., and Bach, W. (2014). Effects of temperature, sulfur, and oxygen fugacity on the composition of sphalerite from submarine hydrothermal vents. *Geology* 42, 699–702. doi:10.1130/g35655.1
- Keith, M., Smith, D. J., Jenkin, G. R. T., Holwell, D. A., and Dye, M. D. (2018). A review of Te and Se systematics in hydrothermal pyrite from precious metal deposits: Insights into oreforming processes. *Ore Geol. Rev.* 96, 269–282. doi:10.1016/j.oregeorev.2017.07.023
- Knipping, J. L., Bilenker, L. D., Simon, A. C., Reich, M., Barra, F., Deditius, A. P., et al. (2015). Trace elements in magnetite from massive iron oxide-apatite deposits indicate a combined formation by igneous and magmatic-hydrothermal processes. *Geochimica Cosmochimica Acta* 171, 15–38. doi:10.1016/j.gca.2015.08.010
- Koglin, N., Frimmel, H. E., Minter, W. L., and Brätz, H. (2010). Trace-element characteristics of different pyrite types in Mesoproterozoic to Palaeoproterozoic placer deposits. *Min. Deposita* 45, 259–280. doi:10.1007/s00126-009-0272-0
- Koski, R. A., Shanks, W. C., III, Bohrsen, W. A., and Oscarson, R. L. (1988). The composition of massive sulfide deposits from the sediment-covered floor of escanaba trough, gorda ridge: Implications for depositional processes. *Can. Mineral.* 26, 655–673.
- Lan, T. G., Fan, H. R., Santosh, M., Hu, F. F., Yang, K. F., Yang, Y. H., et al. (2012). Early jurassic high-K calc-alkaline and shoshonitic rocks from the tongshi intrusive complex, eastern north China craton: Implication for crust-mantle interaction and post-collisional magmatism. *Lithos* 140, 183–199. doi:10.1016/j.lithos.2012.01.015
- Landis, G. P., and Hofstra, A. H. (1991). Fluid inclusion gas chemistry as a potential minerals exploration tool: Case studies from creede, CO, jerritt canyon, NV, coeur d'Alene district, ID and MT, southern Alaska mesothermal veins, and mid-continent MVT's. *J. Geochem. Explor.* 42, 25–59. doi:10.1016/0375-6742(91)90059-4
- Large, R. R., Halpin, J. A., Danyushevsky, L. V., Maslennikov, V. V., Bull, S. W., Long, J. A., et al. (2014). Trace element content of sedimentary pyrite as a new proxy for deep-time ocean-atmosphere evolution. *Earth Planet. Sci. Lett.* 389, 209–220. doi:10.1016/j.epsl.2013.12.020
- Leach, D. L., Landis, G. P., and Hofstra, A. H. (1988). Metamorphic origin of the Coeur d'Alene baseand precious-metal veins in the Belt Basin, Idaho and Montana. *Geol.* 16, 122–125. doi:10.1130/0091-7613(1988)016<0122:mootcd>2.3.co;2
- Li, H. K., Geng, K., Li, Y. F., and Zhuo, C. Y. (2011). Zircon SHRIMP U-Pb age of Tongjing gold deposit in Yinan County, Shandong and its geological significance. *Mineral. Deposits* 30, 497–503. (in Chinese with English abstract).
- Li, J., Song, M. C., Yu, J. T., Bo, J. W., Zhang, Z. L., and Liu, X. (2022). Genesis of Jinqingding Gold Deposit in eastern Jiaodong peninsula, China: Constrains from trace elements of sulfide ore and wall-rock. *Geol. Bull. China* 41, 1010–1022. (in Chinese with English abstract).
- Li, J., Wang, K. Y., Cai, W. Y., Sun, F. Y., Liu, H. L., Fu, L. J., et al. (2020). Triassic gold-silver metallogenesis in Qingchengzi orefield, North China Craton: Perspective from fluid inclusions, REE and H-O-S-Pb isotope systematics. *Ore Geol. Rev.* 121, 103567. doi:10.1016/j.oregeorev.2020.103567
- Li, K., Gu, X. X., and Dong, S. Y. (2009). Isotopic geochemistry of yinan Au-Cu-Fe deposit in shandong province: Mineral deposits. v. 28, no. 1, p. 93–104 (in Chinese with English abstract).
- Li, S. R., and Santosh, M. (2017). Geodynamics of heterogeneous gold mineralization in the North China Craton and its relationship to lithospheric destruction. *Gondwana Res.* 50, 267–292. doi:10.1016/j.gr.2017.05.007
- Lin, J. Q., Tan, D. J., Yu, X. F., Li, B. R., Li, Y., and Xu, W. L. (1997). in *Genesis of the Guilaizhuang gold deposit in western Shandong* (Jinan: Shandong Science and Technology Press), 1–160. (in Chinese with English abstract).
- Liu, Y., Santosh, M., Li, S. R., and Guo, P. (2014). Stable isotope geochemistry and Re-Os ages of the Yi'an gold deposit, Shandong Province, northeastern China. *Int. Geol. Rev.* 6, 695–710. doi:10.1080/00206814.2014.886167

- Liu, Y. S., Hu, Z. C., Gao, S., Günther, D., Xu, J., Gao, C. G., et al. (2008). *In situ* analysis of major and trace elements of anhydrous minerals by LA-ICP-MS without applying an internal standard. *Chem. Geol.* 257, 34–43. doi:10.1016/j.chemgeo.2008.08.004
- Loftus-Hill, G., and Solomon, M. (1967). Cobalt, nickel and selenium in sulphides as indicators of ore Genesis. *Mineral. Deposita* 2, 228–242.
- Ma, Y., Jiang, S. Y., Frimmel, H. E., and Zhu, L. Y. (2022). *In situ* chemical and isotopic analyses and element mapping of multiple-generation pyrite: Evidence of episodic gold mobilization and deposition for the Qiucun epithermal gold deposit in Southeast China. *Am. Mineralogist* 107, 1133–1148. doi:10.2138/am-2022-8030
- Manske, S. L., and Paul, A. H. (2002). Geology of a major new porphyry copper center in the Superior (Pioneer) district, Arizona. *Econ. Geol.* 97, 197–220. doi:10.2113/gsecongeo.97.2.197
- Mao, J. W., Wang, Y. T., Zhang, Z. H., Yu, J. J., and Niu, B. G. (2003). Geodynamic settings of mesozoic large-scale mineralization in north China and adjacent areas—implication from the highly precise and accurate ages of metal deposits. *Sci. China Ser. D.* 46, 838–851. doi:10.1360/03yd0202
- Maslennikov, V. V., Maslennikova, S. P., Large, R. R., and Danyushevsky, L. V. (2009). Study of trace element zonation in vent chimneys from the Silurian Yaman-Kasy volcanic-hosted massive sulfide deposit (Southern Urals, Russia) using laser ablation-inductively coupled plasma mass spectrometry (LA-ICP-MS). *Econ. Geol.* 104, 1111–1141. doi:10.2113/gsecongeo.104.8.1111
- Meinert, L. D., Dippl, G. M., and Nicolescu, S. (2005). World skarn deposits. *Econ. Geol.* 100, 299–366.
- Meinert, L. D. (1992). Skarns and skarn deposits. *Geosci. Can.* 19 (4), 145–162.
- Meng, Y. M., Hu, R. Z., Huang, X. W., Gao, J. F., Qi, L., and Lyu, C. (2018). The relationship between stratabound Pb-Zn-Ag and porphyry-skarn Mo mineralization in the laochang deposit, southwestern China: Constraints from pyrite Re-Os isotope, sulfur isotope, and trace element data. *J. Geochem. Explor.* 194, 218–238. doi:10.1016/j.jexplo.2018.08.008
- Menzies, M. A., Fan, W., and Zhang, M. (1993). Palaeozoic and Cenozoic lithoprobes and the loss of >120 km of Archaean lithosphere, Sino-Korean craton, China. *Geol. Soc. Lond. Spec. Publ.* 76, 71–81. doi:10.1144/gsl.sp.1993.076.01.04
- Mukherjee, I., and Large, R. (2017). Application of pyrite trace element chemistry to exploration for SEDEX style Zn-Pb deposits: McArthur basin, northern territory, Australia. *Ore Geol. Rev.* 81, 1249–1270. doi:10.1016/j.oregeorev.2016.08.004
- Mumin, A. H., Fleet, M. E., and Chryssoulis, S. L. (1994). Gold mineralization in as-rich mesothermal gold ores of the BogosoPrestea mining district of the ashanti gold belt, Ghana: Remobilization of “invisible” gold. *Mineral. Deposita* 29, 445–460. doi:10.1007/bf00193506
- Naden, J., and Henney, P. J. (1995). *Characterisation of gold from Fiji*. Keyworth, Nottinghamshire: British Geological Survey, 1–17. Technical report WC/95/41.
- Nadoll, P., Angerer, T., Mauk, J. L., French, D., and Walshe, J. (2014). The chemistry of hydrothermal magnetite: A review. *Ore Geol. Rev.* 61, 1–32. doi:10.1016/j.oregeorev.2013.12.013
- Nadoll, P., Mauk, J. L., Hayes, T. S., Koenig, A. E., and Box, S. E. (2012). Geochemistry of magnetite from hydrothermal ore deposits and host rocks of the Mesoproterozoic Belt Supergroup, United States. *Econ. Geol.* 107, 1275–1292. doi:10.2113/econgeo.107.6.1275
- Nadoll, P., Mauk, J. L., Leveille, R. A., and Koenig, A. E. (2015). Geochemistry of magnetite from porphyry Cu and skarn deposits in the southwestern United States. *Min. Deposita* 50, 493–515. doi:10.1007/s00126-014-0539-y
- Niu, S. Y., Hu, H. B., Mao, J. W., Sun, A. Q., Xu, C. S., and Hou, Q. L. (2004). Adapting English into Chinese. *Engl. Today* 31, 34–39. (in Chinese with English abstract). doi:10.1017/s0266078404002068
- Niu, X., Shu, Q., Xing, K., Yuan, S., Wei, L., Zhang, Y., et al. (2022). Evaluating Sn mineralization potential at the Haobugao skarn Zn-Pb deposit (NE China) using whole-rock and zircon geochemistry. *J. Geochem. Explor.* 234, 106938. doi:10.1016/j.jexplo.2021.106938
- Ohmoto, H., and Rye, R. O. (1979). “Isotopes of sulfur and carbon,” in *Geochemistry of hydrothermal ore deposits*. Editor H. L. Barnes. second edition (New York: John Wiley), 509–567.
- Papike, J. J., Burger, P. V., Bell, A. S., Shearer, C. K., Le, L., and Jones, J. (2015). Normal to inverse transition in martian spinel: Understanding the interplay between chromium, vanadium, and iron valence state partitioning through a crystal-chemical lens. *Am. Mineralogist* 100, 2018–2025. doi:10.2138/am-2015-5208
- Peng, H. J., Mao, J. W., Hou, L., Shu, Q. H., Zhang, C. Q., Liu, H., et al. (2016). Stable isotope and fluid inclusion constraints on the source and evolution of ore fluids in the Hongniu-Hongshan Cu skarn deposit, Yunnan Province, China. *Econ. Geol.* 111, 1369–1396. doi:10.2113/econgeo.111.6.1369
- Qiu, J. S., Wang, D. Z., and Ren, Q. J. (1996). Geological geochemical characteristics and Genesis of the Jinchang skarn type gold-copper deposit. *Yinan Cty. Shandong Prov. Mineral. Deposits* 15, 330–340. (in Chinese with English abstract).
- Reich, M., Deditius, A., Chryssoulis, S., Li, J. W., Ma, C. Q., Parada, M. A., et al. (2013). Pyrite as a record of hydrothermal fluid evolution in a porphyry copper system: A SIMS/EMPA trace element study. *Geochimica Cosmochimica Acta* 104, 42–62. doi:10.1016/j.gca.2012.11.006
- Reich, M., Kesler, S. E., Utsunomiya, S., Palenik, C. S., Chryssoulis, S. L., and Ewing, R. C. (2005). Solubility of gold in arsenian pyrite. *Geochimica Cosmochimica Acta* 69, 2781–2796. doi:10.1016/j.gca.2005.01.011
- Santosh, M. (2010). Assembling North China craton within the columbia supercontinent: The role of double-sided subduction. *Precambrian Res.* 178, 149–167. doi:10.1016/j.precamres.2010.02.003
- Schirmer, T., Koschinsky, A., and Bau, M. (2014). The ratio of tellurium and selenium in geological material as a possible paleo-redox proxy. *Chem. Geol.* 376, 44–51. doi:10.1016/j.chemgeo.2014.03.005
- SDGG (Shandong Gold Group Co., Ltd.) (2008). *Detailed geological survey report on deep and peripheral Au-Cu mineralization in Tongjing*. Yi’nan County, Shandong Province. (in Chinese).
- SDGM (Shandong Gold Geological Minerals Survey Co. Ltd.) (2015). *Detailed geological survey report of the Tongjing and Jinchang Au-Cu deposits*. Yi’nan County, Shandong Province. (in Chinese).
- Shi, W. J. (2014). *The late mesozoic tectonic-magmatic Evolution Process in the yishu fault zone and adjacent regions, Shandong province: Implication for gold mineralization*. Wuhan: China University of Geosciences for the Doctor Degree, 1–142. (in Chinese with English abstract).
- Shu, Q., Chang, Z., Hammerli, J., Lai, Y., and Huizenga, J.-M. (2017). Composition and evolution of fluids forming the baiyinnuo’er Zn-Pb skarn deposit, northeastern China: Insights from laser ablation ICP-MS study of fluid inclusions. *Econ. Geol.* 112, 1441–1460. doi:10.5382/econgeo.2017.4516
- Shu, Q., Chang, Z., and Mavrogenes, J. (2021). Fluid compositions reveal fluid nature, metal deposition mechanisms, and mineralization potential: An example at the Haobugao Zn-Pb skarn. *China. Geology* 49, 473–477. doi:10.1130/g48348.1
- Shu, Q., Lai, Y., Sun, Y., Wang, C., and Meng, S. (2013). Ore Genesis and hydrothermal evolution of the baiyinnuo’er zinc-lead skarn deposit, northeast China: Evidence from isotopes (S, Pb) and fluid inclusions. *Econ. Geol.* 108, 835–860. doi:10.2113/econgeo.108.4.835
- Sillitoe, R. H. (2010). Porphyry copper systems. *Econ. Geol.* 105, 3–41. doi:10.2113/gsecongeo.105.1.3
- Simmons, S. F., White, N. C., and John, D. A. (2005). Geological characteristics of epithermal precious and base metal deposits. *Econ. Geol.* 100, 485–522.
- Song, K. R., Tang, L., Zhang, S. T., Santosh, M., Spencer, C. J., Zhao, Y., et al. (2019). Genesis of the Bianjiadayuan Pb-Zn polymetallic deposit, Inner Mongolia, China: Constraints from *in-situ* sulfur isotope and trace element geochemistry of pyrite. *Geosci. Front.* 10, 1863–1877. doi:10.1016/j.gsf.2019.02.004
- Song, M. C., and Li, H. K. (2001). Study on regional geological structural evolution in Shandong Province. *Shandong Geol.* 17, 12–21. (in Chinese with English abstract).
- Sung, Y.-H., Brugger, J., Ciobanu, C., Pring, A., Skinner, W., and Nugus, M. (2009). Invisible gold in arsenian pyrite and arsenopyrite from a multi-stage Archaean gold deposit: Sunrise dam, Eastern Goldfields province, Western Australia. *Min. Deposita* 44, 765–791. doi:10.1007/s00126-009-0244-4
- Takeno, N. (2005). Atlas of Eh-pH diagrams: Intercomparison of thermodynamic data bases. *Geol. Surv. Jpn. Open File Rep.* 419, 285.
- Tardani, D., Reich, M., Deditius, A. P., Chryssoulis, S., Sanchez-Alfaro, P., Wragge, J., et al. (2017). Copper-arsenic decoupling in an active geothermal system: A link between pyrite and fluid composition. *Geochimica Cosmochimica Acta* 204, 179–204. doi:10.1016/j.gca.2017.01.044
- Thompson, J. F. H., Sillitoe, R. H., Baker, T., Lang, J. R., and Mortensen, J. K. (1999). Intrusion-related gold deposits associated with tungsten-tin provinces. *Miner. Deposita* 34, 323–334. doi:10.1007/s001260050207
- Thorne, W. S., Hagemann, S. G., Webb, A., and Clout, J. (2008). “Banded iron formation-related iron ore deposits of the Hamersley Province, Western Australia,” in *Banded iron formation-related highgrade iron ore*. Editors S. G. Hagemann, C. A. Rosière, J. Gutzmer, and N. J. Beukes, 197–222.
- Tian, J. X., Li, X. Z., Song, Z. Y., Liu, H. D., Huang, Y. B., and Zhu, D. C. (2015). Environment formation age and material sources of mesozoic gold deposits in Western Shandong a synthesis. *Acta Geol. Sin.* 89, 1530–1537. (in Chinese with English abstract).
- Vaughan, D. J., and Rosso, K. M. (2006). Chemical bonding in sulfide minerals. *Rev. Mineralogy Geochem.* 61, 231–264. doi:10.2138/rmg.2006.61.5
- Voute, F., Hagemann, S. G., Evans, N. J., and Villanes, C. (2019). Sulfur isotopes, trace element, and textural analyses of pyrite, arsenopyrite and base metal sulfides associated with gold mineralization in the pataz-parcoy district, Peru: Implication

- for paragenesis, fluid source, and gold deposition mechanisms. *Min. Deposita* 54, 1077–1100. doi:10.1007/s00126-018-0857-6
- Wan, T. F. (1992). Tectonic evolution and stress field in Shandong province. *Geol. Shandong* 8, 70–101. (in Chinese with English abstract).
- Wan, Y. S., Liu, D. Y., Wang, S. J., Yang, E. X., Wang, W., Dong, C. Y., et al. (2011). ~2.7Ga juvenile crust formation in the North China Craton (Taishan-Xintai area, Western Shandong Province): Further evidence of an understated event from U–Pb dating and Hf isotopic composition of zircon. *Precambrian Res.* 186, 169–180. doi:10.1016/j.precamres.2011.01.015
- Wang, Q. L., Zhang, J. Y., Yan, D. T., Min, H., Liu, S., and Li, C. (2021). Genesis of ore deposits indicated by trace elements of chalcopyrite. *Bull. Geol. Sci. Technol.*, 1–19. (in Chinese with English abstract).
- Wang, Y., Fan, H. R., Hu, F. F., Lan, T. G., Jiao, P., and Wang, S. P. (2011). Zircon U–Pb ages and geochemical characteristics of elements and isotopes of the diorite from Tongjing 'Yinan' Western Shandong Province. *Mineralogy Petrology* 30, 553–566. (in Chinese with English abstract).
- Wang, Y. (2010). *Late Mesozoic magmatism and gold-copper mineralization in the southwestern part of Shandong province*. Ph.D. thesis. Beijing: Chinese Academy of Sciences, 1–199. (In Chinese).
- Wu, F. Y., Lin, J. Q., Wilde, S. A., Zhang, X. O., and Yang, J. H. (2005a). Nature and significance of the Early Cretaceous giant igneous event in Eastern China. *Earth Planet. Sci. Lett.* 233, 103–119. doi:10.1016/j.epsl.2005.02.019
- Wu, F. Y., Yang, J. H., Wilde, S. A., and Zhang, X. O. (2005b). Geochronology, petrogenesis and tectonic implications of Jurassic granites in the Liaodong Peninsula, NE China. *Chem. Geol.* 221, 127–156. doi:10.1016/j.chemgeo.2005.04.010
- Wu, M. L., Zhao, G. C., Sun, M., Li, S. Z., He, Y. H., and Bao, Z. A. (2013). Zircon U–Pb geochronology and Hf isotopes of major lithologies from the Yishui terrane: Implications for the crustal evolution of the eastern block, north China craton. *Lithos* 171, 164–178. doi:10.1016/j.lithos.2013.03.005
- Xie, Q. H., Zhang, Z. C., Hou, T., Jin, Z. L., and Santosh, M. (2017). Geochemistry and oxygen isotope composition of magnetite from the Zhangmatun deposit, North China Craton: Implications for the magmatic-hydrothermal evolution of Cornwall-type iron mineralization. *Ore Geol. Rev.* 88, 57–70. doi:10.1016/j.oregeorev.2017.04.014
- Xu, Y. G., Ma, J. L., Huang, X. L., Izuka, Y., Chung, S. L., Wang, Y. B., et al. (2004). Early Cretaceous gabbroic complex from Yinan, Shandong province: Petrogenesis and mantle domains beneath the North China craton. *Int. J. Earth Sci.* 93, 1025–1041. doi:10.1007/s00531-004-0430-7
- Xu, Y. G. (2001). Thermo-tectonic destruction of the archaean lithospheric keel beneath the Sino-Korean craton in China: Evidence, timing and mechanism. *Phys. Chem. Earth Part A Solid Earth Geodesy* 26, 747–757. doi:10.1016/s1464-1895(01)00124-7
- Xu, Y. G., Wu, X. Y., Luo, Z. Y., Ma, J. L., Huang, X. L., and Xie, L. W. (2007). Zircon Hf isotope compositions of middle Jurassic-early Cretaceous intrusions in Shandong province and its implications. *Acta Petrol. Sin.* 23, 307–316. (in Chinese with English abstract).
- Yang, C. H., Xu, W. L., Yang, D. B., Liu, C. C., Liu, X. M., and Hu, Z. C. (2006). Petrogenesis of the Mesozoic high-Mg diorites in west Shandong: Evidence from chronology and petro-geochemistry. *J. China Univ. Geosciences (Earth Sci.)* 31, 81–92. (in Chinese with English abstract).
- Yang, C. H., Xu, W. L., Yang, D. B., Wang, W., Wang, W. D., and Liu, J. M. (2008). Genesis of Shangyu gabbro diorite in Western Shandong: Evidence from geochronology and petrogeochemistry. *Sci. China Earth Sci.* 01, 44–55. (In Chinese).
- Yang, J. H., Sun, J. F., Zhang, J. H., and Wilde, S. A. (2012). Petrogenesis of Late Triassic intrusive rocks in the northern Liaodong Peninsula related to decratonization of the North China Craton: Zircon U–Pb age and Hf–O isotope evidence. *Lithos* 153, 108–128. doi:10.1016/j.lithos.2012.06.023
- Yang, J. H., Xu, L., Sun, J. F., Zeng, Q., Zhao, Y. N., Wang, H., et al. (2021). Geodynamics of decratonization and related magmatism and mineralization in the North China Craton. *Sci. China Earth Sci.* 64, 1409–1427. doi:10.1007/s11430-020-9732-6
- Yu, X. F., Li, D. P., Li, Z. S., Wei, P. F., and Rana, N. S. S. (2019). Research on geochemical process of Te–Au elements in Guilaizhuang gold deposit of Western Shandong. *Mineral. Deposits* 38, 277–290.
- Zartman, R. E., and Doe, B. R. (1981). Plumbotectonics—the model. *Tectonophysics* 75, 135–162. doi:10.1016/0040-1951(81)90213-4
- Zeng, Q. D., Liu, J. M., Qin, K. Q., Fan, H. R., Chu, S. X., Wang, Y. B., et al. (2013). Types, characteristics, and time-space distribution of molybdenum deposits in China. *Int. Geol. Rev.* 55, 1311–1358. doi:10.1080/00206814.2013.774195
- Zeng, Q. D., Wang, Y. B., Yang, J. H., Guo, Y. P., Yu, B., Zhou, L. L., et al. (2020). Spatial-temporal distribution and tectonic setting of gold deposits in the northern margin gold belt of the North China Craton. *Int. Geol. Rev.* 63, 941–972. doi:10.1080/00206814.2020.1737839
- Zhai, M. G. (2011). Cratonization and the ancient north China continent: A summary and review. *Sci. China Earth Sci.* 54, 1110–1120. doi:10.1007/s11430-011-4250-x
- Zhai, M. G., and Santosh, M. (2011). The early Precambrian odyssey of the North China craton: A synoptic overview. *Gondwana Res.* 20, 6–25. doi:10.1016/j.gr.2011.02.005
- Zhang, C., Cui, F. H., and Geng, R. (2021). The petrogenesis of early Cretaceous quartz diorite in skarn iron deposits, Jinling area, Luxi: Evidence of geochronology and geochemistry. *Mineralogy Petrology* 41, 80–92. (in Chinese with English abstract).
- Zhang, W., Hu, Z. C., Gunther, D., Liu, Y. S., Ling, W. L., Zong, K. Q., et al. (2016). Direct lead isotope analysis in Hg-rich sulfides by LA-MC-ICP-MS with a gas exchange device and matrix-matched calibration. *Anal. Chim. Acta* 948, 9–18. doi:10.1016/j.aca.2016.10.040
- Zhang, W., Hu, Z. C., and Liu, Y. S. (2020). Iso-compass: New freeware software for isotopic data reduction of LA-MC-ICP-MS. *J. Anal. At. Spectrom.* 35, 1087–1096. doi:10.1039/d0ja00084a
- Zhang, Y. Y., Zhen, S. M., Wang, D. Z., Liu, J. J., Wang, J., Zha, Z. J., et al. (2022). *In situ* trace elements and sulfur isotopes of sulfides in the Dabaiyang Te–Au deposit, Hebei Province, China: Implications for Au remobilization from pyrite. *Ore Geol. Rev.* 140, 104626. doi:10.1016/j.oregeorev.2021.104626
- Zhang, Z. R., and Chen, M. X. (1995). The application of the gold fineness research in geology. *Gold Sci. Technol.* 3, 21–24. (in Chinese).
- Zhao, G. C., and Cawood, P. A. (2012). Precambrian geology of China. *Precambrian Res.* 222, 13–54. doi:10.1016/j.precamres.2012.09.017
- Zhao, G. C., Sun, M., Wilde, S. A., and Li, S. Z. (2005). Late archaean to paleoproterozoic evolution of the North China craton: Key issues revisited. *Precambrian Res.* 136, 177–202. doi:10.1016/j.precamres.2004.10.002
- Zhao, G. C., Wilde, S. A., Cawood, P. A., and Sun, M. (2001). Archaean blocks and their boundaries in the North China Craton: Lithological, geochemical, structural and P–T path constraints and tectonic evolution. *Precambrian Res.* 107, 45–73. doi:10.1016/s0301-9268(00)00154-6
- Zhao, W. W., and Zhou, M. F. (2015). *In-situ* LA-ICP-MS trace elemental analyses of magnetite: The Mesozoic tectonic Fe deposit in the Nanling range south China. *Ore Geol. Rev.* 65, 872–883. doi:10.1016/j.oregeorev.2014.09.019
- Zhu, D. C., Tian, R. C., Tian, J. X., Yu, X. F., Yang, Z. Y., and Yang, S. P. (2018). He–Ar isotopic determination of skarn type copper gold deposits in western Shandong and its geological significance—taking Tongjing type copper gold deposits in Yinan area as an example. *Shandong Land Resour.* 34, 1–5. (in Chinese with English abstract).
- Zhu, G., Jiang, D. Z., Zhang, B. L., and Chen, Y. (2012). Destruction of the Eastern North China Craton in a backarc setting: Evidence from crustal deformation kinematics. *Gondwana Res.* 22, 86–103. doi:10.1016/j.gr.2011.08.005
- Zhu, J. (2014). *Geochronology, Metallogenic model and ore prospecting of the Guilaizhuang gold deposit, west of Shandong province*. Beijing: China University of Geosciences for the master Degree, 1–78. (in Chinese with English abstract).
- Zhu, R. X., Chen, L., Wu, F. Y., and Liu, J. L. (2011). Timing, scale and mechanism of the destruction of the North China Craton. *Sci. China Earth Sci.* 54, 789–797. doi:10.1007/s11430-011-4203-4
- Zierenberg, R. A., Koski, R. A., Morton, J. L., Bouse, R. M., and Shanks, W. C., III (1993). Genesis of massive sulfide deposits on a sediment-covered spreading center, Escanaba Trough, Southern Gorda Ridge. *Econ. Geol.* 88, 2069–2098. doi:10.2113/gsecongeo.88.8.2069